

Article

New Power Quality Indices for the Assessment of Waveform Distortions from 0 to 150 kHz in Power Systems with Renewable Generation and Modern Non-Linear Loads

Luisa Alfieri ^{1,*} , Antonio Bracale ²  and Anders Larsson ³

¹ Department of Electrical Engineering and Information Technology, University of Naples Federico II, Via Claudio, 21, 80125 Naples, Italy

² Department of Engineering, University of Naples Parthenope, Centro Direzionale of Naples, Is C4, 80143 Naples, Italy; antonio.bracale@uniparthenope.it

³ Department of Engineering Sciences and Mathematics, Luleå University of Technology, 971 87 Luleå, Sweden; anders.1.larsson@ltu.se

* Correspondence: luisa.alfieri@unina.it; Tel.: +39-081-768-3203

Received: 7 June 2017; Accepted: 10 October 2017; Published: 17 October 2017

Abstract: The widespread use of power electronics converters, e.g., to interface renewable generation systems with the grid or to supply some high-efficiency loads, has caused increased levels of waveform distortions in the modern distribution system. Voltage and current waveforms include spectral components from 0 kHz to 150 kHz, characterized by a non-uniform time-frequency behavior. This wide interval of frequencies is currently divided into “low-frequency” (from 0 kHz to 2 kHz) and “high-frequency” (from 2 kHz to 150 kHz). While the low-frequencies have been exhaustively investigated in the relevant literature and are covered by adequate standardization, studies for the high-frequencies have been addressed only in the last decade to fill current regulatory gaps. In this paper, new power quality (PQ) indices for the assessment of waveform distortions from 0 kHz to 150 kHz are proposed. Specifically, some currently available indices have been properly modified in order to extend their application also to wide-spectrum waveforms. In the particular case of waveform distortions due to renewable generation, numerical applications prove that the proposed indices are useful tools for the characterization of problems (e.g., overheating, equipment malfunctioning, losses due to skin effects, hysteresis losses or eddy current losses) in cases of both low-frequency and high-frequency distortions.

Keywords: power quality indices; waveform distortions; high-frequency spectral components; fluorescent lamps; renewable generation

1. Introduction

The widespread use of power electronics converters in the modern distribution system is among the main causes of waveform distortions in power systems. Power electronics converters are utilized both to interface distributed energy resources with the grid and to supply some high-efficiency loads (e.g., adjustable speed drives, LED and fluorescent lamps). With particular reference to dispersed generation by renewable primary sources, the rising diffusion of photovoltaic systems and wind turbine systems, usually interfaced by means of power electronics converters, is becoming one of the main causes of spectral emissions, and has a significant impact on abnormal conditions in distribution networks.

These abnormal conditions determine voltage and current waveforms characterized by the presence of continuous disturbances including a spectral content in a wide interval of frequencies (from 0 kHz to 150 kHz), with non-uniform behavior both in time and in frequency [1–3].

Within this wide range of frequencies, “low-frequency components” and “high-frequency components” have been identified in order to separate the distortions in the range from 0 kHz to 2 kHz and from 2 kHz to 150 kHz, respectively. This definition is true only for 50 Hz systems. According to the IEC standards, for 60 Hz systems, the low-frequency range is from 0 Hz to 2.4 kHz, while the high-frequency range is from 2.4 kHz up to 150 kHz. These two ranges of frequencies gather spectral components with similar features, which can be summarized as follows [1,4,5]:

- low-frequency distortions are often slowly time-varying, while high-frequency distortions usually have both amplitudes and frequencies that are highly variable in time;
- low-frequency distortions tend to propagate toward the grid, while high-frequency distortions mainly circulate inside the installations;
- the low-frequency range is currently covered by adequate standardizations that indicate indices, limits and spectral analysis methods for a proper evaluation of such disturbances. Conversely, the high-frequency range is still not standardized, although many working groups have been instituted by international setting standard organizations with the aim of investigating this issue.

With reference to the first point, it is clear that an accurate evaluation of the spectral content versus time should take into account the different behaviors of variability of low-frequency and high-frequency distortions. In addition, it should be recalled that the period of low-frequency spectral components naturally includes the periods of each high-frequency spectral component several times. As a consequence of these considerations, the following problems arise:

- i. novel and appropriate methods for the spectral analysis (such as time-frequency representations) should be utilized. They must be able to use different sliding time window lengths for the different ranges of frequencies. In particular, longer sliding windows for low-frequency components and shorter sliding windows for high-frequency components should be used;
- ii. time and frequency resolutions of spectra should not be linked one each other in order to maximize the accuracy of results in both domains;
- iii. methodologies for synchronizing information coming from the analysis of low-frequency and high-frequency ranges and their relative spectral components should be addressed.

With reference to the propagation characteristics of low-frequency and high-frequency distortions, different problems and effects on the electrical power system devices can arise inside the installation or in distribution systems due to the presence of power electronics converters. So, the introduction of novel power quality (PQ) indices specifically tailored to these wide-spectrum waveforms are useful for characterizing the disturbances in the low-frequency and high-frequency ranges in different ways.

Eventually, with reference to the lack of standardization for the high-frequency range, it is worth observing that, although some International Special Committee on Radio Interference (CISPR) standards (e.g., CISPR 14 and 15 [6]) address the regulation of the emissions up to 150 kHz of some typology of equipment, no general limits either for emission or immunity levels have been defined. Moreover, the International Electrotechnical Commission (IEC) standards currently only address waveform distortion assessment in a range from 0 kHz to 9 kHz, recommending the use of the discrete Fourier transform (DFT) with a rectangular time window of fixed duration (a fundamental period of 10 or 12 cycles for 50 Hz or 60 Hz systems, respectively) that slides along the waveform in time, performing a short time Fourier transform (STFT) [7,8]. Inaccuracies due to spectral leakage and inherent frequency resolution can occur using STFT, so IEC standards propose grouping evaluation. As a demonstration of the importance of the high-frequency range assessment, the IEC standards recently suggested the extension of the grouping, originally defined from 2 kHz to 9 kHz, up to 150 kHz, although only for informative, rather than normative, purposes [8].

However, both normative and informative IEC methods only provide a global evaluation of waveform distortions, omitting any detailed information about each spectral component. For this and other reasons, the IEC standards encourage the individuation of other techniques for the analysis of the high-frequency range, and warn that other methods could be included in future editions of the standards.

The need for adequate spectral analysis methods, PQ indicators and standards has become an important issue in recent years. Recently, some methods specifically addressing the detection of waveform distortion throughout the whole range from 0 kHz to 150 kHz have been proposed in the relevant literature [4,9]. Among these, the sliding-window wavelet-modified estimation of signal parameters by rotational invariance technique (ESPRIT) method (SWWMEM) presented in [4] was successfully applied to provide an accurate estimation of both low-frequency and high-frequency spectral components, while requiring an acceptable computational burden. In particular, SWWMEM utilizes a discrete wavelet transform (DWT) for the decomposition of the wide-spectrum waveform into a low-frequency waveform (including spectral content from 0 kHz to 2 kHz) and a high-frequency waveform (including spectral content from 2 kHz to 150 kHz). Then, low- and high-frequency waveforms are separately analyzed by a sliding-window modified ESPRIT method, with proper selection of the duration of the analysis window for each waveform. In our opinion, this method is particularly interesting, since it allows a detailed evaluation of the high-frequency content and, therefore, can also be applied for the definition of new PQ indices, aimed at filling out the current lack of regulation for the high-frequency range [10–12].

When dealing with new PQ indices, one must take into account that the indices should be powerful tools for quickly quantifying a PQ disturbance with a single number. They should assess compliance with the required standards or recommendations within a given regulatory framework, and illustrate the negative effects of electrical disturbances on power system components [13].

The effects of low-frequency waveform distortions are well known [3,13]. In the case of high-frequency distortions, it was recently demonstrated that they can determine significant detrimental effects on the electrical power system devices [14]. For example, problems can occur since: (i) equipment malfunctioning or behaving in undesirable ways (e.g., clocks running too fast, hair dryers turning on by themselves, and flickering lights) could cause incidents; (ii) audible noise due to stimulation of a mechanical resonance and perceptible by humans could be produced in high-frequency ranges up to 20 kHz, and audible noise perceptible by animals could be determined at even higher frequencies; (iii) the electrolyte capacitors could be damaged by high-frequency currents led by high-frequency voltages; (iv) high-frequency currents also could contribute to the heating of electrical devices, causing life reduction for them and, consequently, damage to different entities throughout the whole installation; (v) the cables could be affected by higher conduction losses due to skin effects; and/or (vi) the ferromagnetic core losses in electrical machines and transformers, depending on the frequency (i.e., hysteresis losses) and on the squared frequency (i.e., eddy current losses), could significantly grow [14].

Hence, these emerging problems due to high-frequency distortions require indices and adequate limits, in order to guarantee the containment of the aforementioned negative effects.

Motivated by the above, the aim of this paper is to propose new PQ indices for the assessment of waveform distortions for the whole range from 0 kHz to 150 kHz. Specifically, we properly modify currently available indices with the aim to extend their application to the field of wide-spectrum waveforms. These available indices are proposed in [15,16]; these indices were defined using various distributions generalized by Cohen's class or the adaptive Prony's method, respectively, and (i) they provide the time and frequency localization of disturbances; (ii) they provide useful information about the time-varying mapping of the not-stationary disturbances for assessment purposes; (iii) they are useful for characterizing the disturbance in terms of energy and frequency deviations; (iv) they provide an assessment and detection of discrete and continuous disturbances; and (v) they are able to

provide synthetic information about the disturbances by evaluating the mean value of each index over a selected time interval, such as the “principal average” proposed in [15,16].

Starting from these indices, in this paper, we propose new PQ indices based on the time frequency representation obtained applying the sliding-window wavelet-modified ESPRIT method (SWWMEM). These are:

- the short time disturbance energy index for both the low- and high-frequency ($STDE_l$ and $STDE_h$, respectively);
- the short time frequency deviation difference index for both the low- and high-frequency ($\Delta STFD_l$, $\Delta STFD_h$, respectively);
- the short time k-factor difference index for both the low- and high-frequency (ΔSTK_l and ΔSTK_h , respectively).

All of these indices can be easily evaluated once the spectral components obtained by the application of SWWMEM are known. Moreover, they provide useful complementary information about the nature of the spectral content included in the analyzed waveform; e.g., if the high-frequency spectral components in a waveform are characterized by negligible amplitudes at frequencies near to the upper bound of the high-frequency range, $STDE_h$ will have a low value, while $\Delta STFD_h$ and ΔSTK_h will be very high. These new PQ indices can be easily calculated, once the spectral components versus time of the waveform under study are known. Even if they are fully suitable for diagnostic purposes or post processing, the use of these indices in real time practical applications can be limited due to (a) high computational time in the evaluation of the spectral components versus time, in case of highly time-varying waveform distortions; and (b) high cost of measurement devices due to the sampling frequencies, which have to be high enough to allow an accurate evaluation of high-frequency spectral components. In any case, it has the following advantages in comparison to the currently available indices:

- the above advantages from (i) to (v) are extended to wide-spectrum waveforms including high frequency distortions;
- low-frequency and high-frequency disturbances can be evaluated by using PQ indices which can be calculated using different sliding time window lengths leading to more adequate quantification of disturbances;
- SWWMEM may be applied to the whole wide-spectrum waveform, from which all the quantities needed for the calculation of the new PQ indices are provided;
- the analyzed waveform can be classified, since an assessment of the main disturbance allocation between low-frequency and high-frequency distortions is provided.

The paper is organized as follows. Section 2 presents an overview of the high-frequency distortions in power systems. Section 3 provides a theoretical definition of the proposed indices. Numerical applications are included in Section 4. Our conclusions are in Section 5. Finally, the main features of the SWWMEM are reviewed in Appendix A, for the sake of clarity.

2. High-Frequency Distortions in Power Systems

Nowadays, the growing use of devices equipped with power electronics converters in power systems is the main cause of waveform distortion disturbances. These converters can be sources of currents characterized by spectral components in a wide range of frequencies, up to 150 kHz [2–4,11,14]. In particular, spectral content from 2 kHz up to 150 kHz was initially designated as “high-frequency distortion”, but recently the term “supraharmonic” has been more frequently used [17,18]. A detailed list of common devices that are sources of supraharmonics is provided in the relevant literature [14]; they include both loads and generators.

High-frequency distortions are distinguished between primary and secondary emissions. The former refer only to disturbances caused by the considered load or generator power electronics

converters, while the latter refer to disturbances caused by other sources near the considered equipment. Furthermore, several studies have demonstrated that high-frequency emissions are characterized by different propagation in power systems in comparison to low-frequency emissions. In particular, the latter tend to propagate towards the distribution network, while the former mainly flow within the installation [4,14].

With regard to renewable generation, photovoltaic systems (PVSs) and wind turbine systems (WTSs) are the most used technologies and, as shown in Figure 1, they are usually connected to the grid through power static converters, causing high-frequency spectral components as primary emissions as a result of the interfacing converters. Figure 1a shows one of the most diffuse topology solutions for the PVSs: a single-stage PVS. The PV panels identify the PV generator, which is connected to the direct current (DC) side of an inverter, controlled through a PWM technique. The output on the inverter alternating current (AC) side is filtered, and the connection to the distribution network realized through a transformer [19].

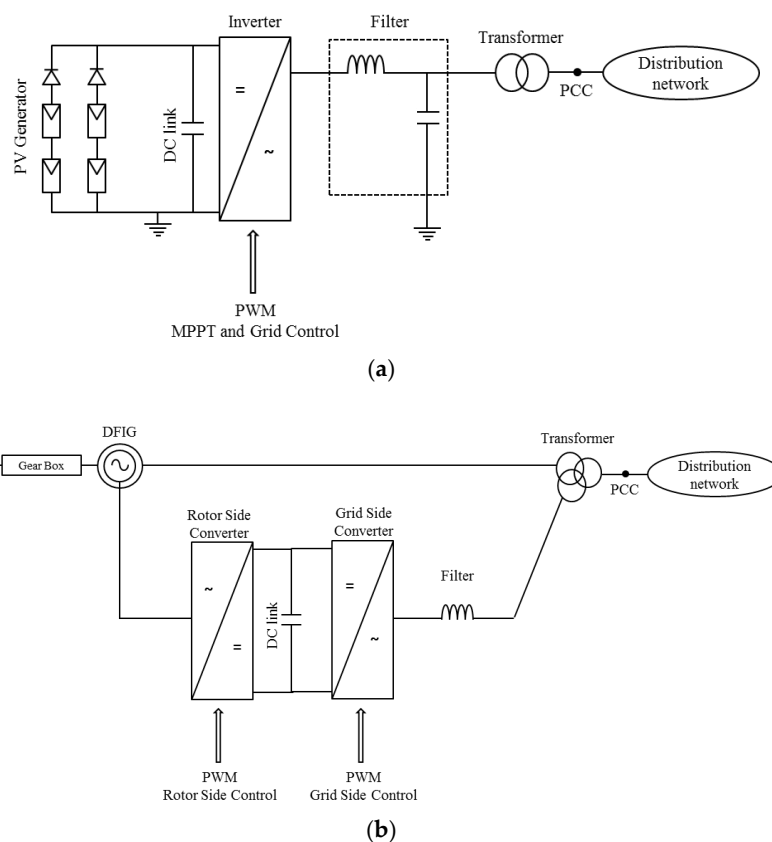


Figure 1. Block scheme of: (a) a photovoltaic system (PVS) and (b) a wind turbine system (WTS).

In PVSs, high-frequency primary emission is linked to the adopted pulse width modulation (PWM) technique of the inverter, although often the presence of an electromagnetic interference filter, used to reduce the harmonic emission, influences the amplitude of the high-frequency components with reference to an ideal PWM spectrum [20]. In case of ideal voltage supply, the high-frequency components can be detected in correspondence with the frequencies $f_{k,m}^{PWM} = [k \cdot f_{sw} \pm m \cdot f_0] \forall k \in \mathbb{N}, \forall m \in \mathbb{N}_0$, where f_{sw} is the switching frequency and f_0 is the power system fundamental frequency. They are sidebands centered on integer multiples of the switching frequency, which is generally a few tens of kHz. The high-frequency secondary emissions in PVSs are due to background voltage distortions or to power line communication (PLC). PLCs are generally in the range from 9 kHz to 95 kHz.

In WTSs, the most diffuse schemes are the doubly fed induction generator (DFIG) and the full-scale power converter wind turbine [21]. Both schemes include power electronics converters which are the main source of high-frequency primary emissions at the point of common coupling (PCC). In particular, the heaviest high-frequency distortions are introduced in the presence of DFIG, whose block scheme is in Figure 1b. In Figure 1b, a variable speed WT with a gearbox and a back-to-back partial scale static converter on the rotor circuit are visible. Moreover, while the stator windings are directly connected to the grid through the transformer, the rotor windings are also fed through a power electronics converter, whose rated power is about 30% of the generator power [22]. So, in this WTS configuration, the power electronics converter with a PWM carrier in the range of a few kHz is on the rotor side of an induction generator. The rotor side operates at a frequency corresponding to the slip of the wind generator, so the high-frequency spectral components due to the PWM are shifted on the stator side by a value that depends both on the grid and slip frequencies. Hence, for such types of WTS, because of the double feeding, the high-frequency spectral components both of the rotor and stator side are injected at the PCC. Additionally, for WTSs, the high-frequency secondary emissions are due to background voltage distortions and PLC [23].

With reference to load emissions, the most diffuse disturbing devices are currently fluorescent lamps powered by high-frequency ballast and the LED lamps [4,17]. Usually, an electronic ballast and an inverter introduce harmonics and spectral components linked to switching frequencies from 30 kHz to 40 kHz. Once again, the high-frequency secondary emissions at the PCC of the considered loads are generally caused by background voltage or by the presence of several disturbing loads in the same installation.

Note that the interaction between supraharmmonic sources makes the high-frequency distortions a heterogeneous set that includes: (i) spectral components with constant frequencies and amplitudes; (ii) spectral components with constant frequencies and varying amplitudes; (iii) spectral components with varying frequencies and amplitudes; and (iv) time-limited broadband signals (i.e., transients and spikes) [9]. This clarifies better the statements in the Section 1 about the requirements in terms of proper selection of the duration of analysis window, and in terms of adequate PQ indices specifically addressed to waveforms that include both low-frequency and high-frequency distortions.

3. Proposed PQ Indices

Among the PQ indices currently available in relevant literature, the short time disturbance energy index (STDE), the short time frequency deviation index (STFD) and the short time k-factor index (STK) defined in [15] present features that make their extension for the characterization of wide-spectrum waveforms interesting. For sake of clarity, we also recall that, for a fixed analysis window, STDE is the ratio between the energy related to the waveform without the fundamental component and the energy related to the only fundamental component; STFD is the ratio between the sum of the energy related to each spectral component included in the waveform, weighted with the corresponding frequency, and the energy related to the whole waveform; STK is the ratio between the sum of the energy related to each spectral component included in the waveform, weighted with the corresponding squared normalized frequency, and the energy related to the whole waveform.

Let $x(n)$ be a N -point sampled distorted power system waveform with a wide-spectrum, with sampling rate f_s ; the decomposition (1) is possible for each sample:

$$x(n) = x_l(n) + x_h(n) = x_o(n) + x_{ld}(n) + x_h(n), n = 0, 1, \dots, N - 1 \quad (1)$$

where $x_l(n)$ includes only the spectral content from 0 kHz to 2 kHz of the original sampled waveform, $x_h(n)$ includes only the spectral content from 2 kHz to 150 kHz of the original sampled waveform, $x_o(n)$ is the sampled fundamental component of the original sampled waveform and $x_{ld}(n) = x_l(n) - x_o(n)$.

Using the SWWMEM [4] and selecting a proper length $L_i \leq N$ of the analysis window for each of the low- and high-frequency waveforms ($i = l, h$), an approximation $\hat{x}_i(n)$ of each sample of $x_l(n)$ and $x_h(n)$ is given by the ESPRIT model in Equation (2), neglecting the additive white noise:

$$\hat{x}_i(n) = \sum_{k=1}^{M_i} A_{ik} e^{j\psi_{ik}} e^{(\alpha_{ik} + j2\pi f_{ik})nT_{si}}, \quad n = 0, 1, \dots, L_i - 1, \quad i = l, h \quad (2)$$

where, for each x_i waveform, M_i is the number of complex exponentials, T_{si} is the sampling period and A_{ik} , α_{ik} , f_{ik} and ψ_{ik} are the amplitude, the damping factor, the frequency, and the initial phase of the k -th exponential, respectively. Note that for $i = l$ and $k = k_o$, the approximation offered by Equation (2) provides $\hat{x}_o(n)$, that assumes the following expression:

$$\hat{x}_o(n) = A_{lk_o} e^{j\psi_{lk_o}} e^{(\alpha_{lk_o} + j2\pi f_{lk_o})nT_{sl}}, \quad n = 0, 1, \dots, L_l - 1 \quad (3)$$

The aforesaid decomposed analysis allows the adequate redefinition of the PQ indices proposed in [15,16] for their application in the field of wide-spectrum waveforms, guaranteeing an estimation of both the low- and high-frequency content compatible with their time-frequency behavior. Specifically, as previously stated, the short time disturbance energy index (STDE), the short time frequency deviation index (STFD) and the short time k-factor index (STK) presented in [15] seem to be particularly useful for the abovementioned application, since they are characterized by: (i) a short-time computation that is more compatible with the non-stationary behavior of the high-frequency disturbances than other PQ indices such as, e.g., the total harmonic distortion (THD), grouping and the distortion index (DIN); (ii) the identification and separation of the energy associated with the fundamental component from that related to the disturbance; (iii) the need of detailed information about each spectral component constituting the disturbance. In fact:

- the STDE is a short-time version of the THD, but, differently from the THD, it performs the distortion quantification by taking into account the energy related not only to the harmonics, but to the whole spectral content included in the waveform;
- the STFD provides a measure of the severity of the highly varying disturbances, weighting each frequency included in the waveform spectrum with the energy content corresponding to that spectral component, in order to estimate the deviation of the instantaneous frequency of the waveform from the power system frequency;
- the STK is the generalization of the k-factor to the whole spectral content included in a waveform, and it is commonly utilized for transformer rating. It is evaluated by weighting the energy density of each spectral component by the square of the normalized frequency.

Based on the aforesaid hints, an adequate manipulation of these selected indices could be suitable for providing information related to the problems listed in Section 1 due to voltage and current waveforms that include both low- and high-frequency spectral content. In particular, the proposed indices that descend from the STDE, evaluated both for the low- and high-frequency ($STDE_l$ and $STDE_h$ indices, respectively), can be utilized to take into account the contribution offered by low- and high-frequency distortions to overheating and, consequently, to life reduction of electrical devices. Similarly, the proposed indices that descend from STFD and STK ($\Delta STFD_h$, ΔSTK_l and ΔSTK_h indices, respectively) can be utilized to take into account the contribution offered by low- and high-frequency distortions to the skin effect, to hysteresis losses, and to eddy current losses.

In the following, the definition of all of the proposed indices is provided in detail. Specifically, the extension of STDE for wide-spectrum waveforms is very intuitive, since it simply relies on the separate evaluation of the definition provided in [15] for the low-frequency ($STDE_l$) and high-frequency ($STDE_h$) range as follows:

$$STDE_l(v_l) = \left\{ \frac{\sum_{k=1, k \neq k_0}^{M_l} \sum_{n=0}^{L_l-1} |A_{lk} e^{j\psi_{lk}} e^{(\alpha_{lk} + j2\pi f_{lk})nT_{sl}}|^2}{\sum_{n=1}^{L_l} |A_{lk_0} e^{j\psi_{lk_0}} e^{(\alpha_{lk_0} + j2\pi f_{lk_0})nT_{sl}}|^2} \right\}^{1/2}, \tag{4}$$

$$STDE_h(v_h) = \left\{ \frac{\sum_{k=1}^{M_h} \sum_{n=0}^{L_h-1} |A_{hk} e^{j\psi_{hk}} e^{(\alpha_{hk} + j2\pi f_{hk})nT_{sh}}|^2}{R_w \cdot \sum_{n=0}^{L_l-1} |A_{lk_0} e^{j\psi_{lk_0}} e^{(\alpha_{lk_0} + j2\pi f_{lk_0})nT_{sl}}|^2} \right\}^{1/2} \tag{5}$$

where $v_i = 1, \dots, N/(f_s L_i T_{si})$ ($\forall i = l, h$) in absence of overlap between consecutive windows, and $R_w = \frac{L_h \cdot T_{sh}}{L_l \cdot T_{sl}}$ is the ratio between low-frequency and high-frequency waveforms time durations with $L_l \cdot T_{sl} > L_h \cdot T_{sh}$, since, as previously stated, the durations of the time windows utilized for the analysis of low- and high-frequency waveforms have to be properly chosen by taking into account the different time-frequency behaviors of the two ranges of frequencies. Moreover, $1/R_w$ has to be an integer number, so, rigorously, the following relationship should be verified $L_l \cdot T_{sl} = \lambda \cdot L_h \cdot T_{sh}$ with $\lambda \in \mathbb{N}$, and, in practical applications, $\frac{1}{R_w} = \frac{L_l \cdot T_{sl}}{L_h \cdot T_{sh}}$ has to be guaranteed. However, the aforesaid observations imply longer sliding windows have to be used for $x_l(n)$, and shorter sliding windows have to be used for $x_h(n)$. In particular, the selection of the analysis window duration should be effected on the basis of the following considerations: (i) the sliding window length has to be longer than (or equal to) the period of the spectral component characterized by the lowest frequency of interest (e.g., 0.02 s in the low-frequency range, and 0.5 ms for the high-frequency range); (ii) the use a short window length (i.e., instantaneous approach) leads to more information and denser evaluation of waveform disturbances, while a long window length (i.e., late approach) provides averaged values of PQ indices and a reduced amount of data [4].

Conversely, the other proposed indices descending from the STFD and STK require more manipulation, since their aim slightly differs from that of the STFD and STK in [15]. For example, the STFD original aim, that is, the instantaneous knowledge of the frequency of the waveform, could be of less interest for wide-spectrum applications than the evaluation of an index that characterizes the influence of the low- and high-frequency disturbances on effects depending linearly on the frequency, for example, the hysteresis losses. This observation leads to the definition of the STFD difference index ($\Delta STFD$) for low- and high-frequency distortions ($\Delta STFD_l$ and $\Delta STFD_h$, respectively).

The starting point for obtaining these proposed indices is the redefinition of STFD for only low-frequency distortions ($STFD_l$) as in Equation (6):

$$STFD_l(v_l) = \frac{\sum_{k=1}^{M_l} f_{lk} \sum_{n=0}^{L_l-1} |A_{lk} e^{j\psi_{lk}} e^{(\alpha_{lk} + j2\pi f_{lk})nT_{sl}}|^2}{\sum_{k=1}^{M_l} \sum_{n=0}^{L_l-1} |A_{lk} e^{j\psi_{lk}} e^{(\alpha_{lk} + j2\pi f_{lk})nT_{sl}}|^2 + \sum_{v_h \in \Omega_{v_l}} \sum_{k=1}^{M_h} \sum_{n=0}^{L_h-1} |A_{hk} e^{j\psi_{hk}} e^{(\alpha_{hk} + j2\pi f_{hk})nT_{sh}}|^2} \tag{6}$$

where Ω_{v_l} is the ensemble of $1/R_w$ elements, representing the high-frequency analysis windows v_h included in a specific low-frequency analysis window v_l .

Then, separating the fundamental contribution in the numerator of Equation (6), the following expression is obtained:

$$STFD_l(v_l) = \frac{f_{lk_0} \sum_{n=0}^{L_l-1} |A_{lk_0} e^{j\psi_{lk_0}} e^{(\alpha_{lk_0} + j2\pi f_{lk_0})nT_{sl}}|^2 + \sum_{k=1, k \neq k_0}^{M_l} f_{lk} \sum_{n=0}^{L_l-1} |A_{lk} e^{j\psi_{lk}} e^{(\alpha_{lk} + j2\pi f_{lk})nT_{sl}}|^2}{\sum_{k=1}^{M_l} \sum_{n=0}^{L_l-1} |A_{lk} e^{j\psi_{lk}} e^{(\alpha_{lk} + j2\pi f_{lk})nT_{sl}}|^2 + \sum_{v_h \in \Omega_{v_l}} \sum_{k=1}^{M_h} \sum_{n=0}^{L_h-1} |A_{hk} e^{j\psi_{hk}} e^{(\alpha_{hk} + j2\pi f_{hk})nT_{sh}}|^2} \tag{7}$$

Bringing the contribution of the fundamental in Equation (7) to the first member, $\Delta STFD_l$ index can be introduced, in order to exclusively quantify the impact of the low-frequency distortions on typical frequency-based problems:

$$\Delta STFD_l(v_l) = \frac{\sum_{k=1, k \neq k_0}^{M_l} f_{lk} \sum_{n=0}^{L_l-1} |A_{lk} e^{j\psi_{lk}} e^{(\alpha_{lk} + j2\pi f_{lk})nT_{sl}}|^2}{\sum_{k=1}^{M_l} \sum_{n=0}^{L_l-1} |A_{lk} e^{j\psi_{lk}} e^{(\alpha_{lk} + j2\pi f_{lk})nT_{sl}}|^2 + \sum_{v_h \in \Omega_{v_l}} \sum_{k=1}^{M_h} \sum_{n=0}^{L_h-1} |A_{hk} e^{j\psi_{hk}} e^{(\alpha_{hk} + j2\pi f_{hk})nT_{sh}}|^2} \tag{8}$$

Note that the aim of all of the proposed indices is to quantify the number of problems related to the presence of waveform distortions both at low-frequency and at high-frequency, in order also to individuate the possible approaches required for their containment. The exclusion of the fundamental component at the numerator of the proposed indices is finalized to avoid its high energy content masking or changing the information of interest to us.

Hence, it is intuitive that the final expression in Equation (8) is directly related only to the contribution made by low-frequency content to the losses that are linearly dependent on frequency value, since it is the sum of the relative energy associated with each low-frequency component of the distortion, multiplied by the corresponding frequency value. Similarly to the expression in Equation (8), the $\Delta STFD_h$ index can also be defined as:

$$\Delta STFD_h(v_h) = \frac{\sum_{k=1}^{M_h} f_{hk} \sum_{n=0}^{L_h-1} |A_{hk} e^{j\psi_{hk}} e^{(\alpha_{hk} + j2\pi f_{hk})nT_{sh}}|^2}{R_w \cdot \sum_{k=1}^{M_l} \sum_{n=0}^{L_l-1} |A_{lk} e^{j\psi_{lk}} e^{(\alpha_{lk} + j2\pi f_{lk})nT_{sl}}|^2 + \sum_{k=1}^{M_h} \sum_{n=0}^{L_h-1} |A_{hk} e^{j\psi_{hk}} e^{(\alpha_{hk} + j2\pi f_{hk})nT_{sh}}|^2} \quad (9)$$

Similarly, $\Delta STFD_h$ provided by Equation (9) is the sum of the relative energy associated with each high-frequency component of the distortion multiplied by the corresponding frequency value, so it identifies the contribution of the high-frequency content to losses that are linearly dependent on frequency value.

Finally, the definition of the proposed indices that descend from STK also follows the same approach as that utilized for $\Delta STFD_l$ and $\Delta STFD_h$. In particular, being interested in the quantification of the influence of both low- and high-frequency disturbance on effects that are dependent on the squared frequencies (for example, Joule losses), the STK difference index (ΔSTK) is proposed.

So, starting from an evaluation of the STK for the low-frequency (STK_l) and performing manipulations similar to those shown for the $\Delta STFD_l$ index, the ΔSTK_l and ΔSTK_h indices, for the low- and high-frequency range, respectively, were also evaluated as follows:

$$\Delta STK_l(v_l) = \frac{\sum_{k=1, k \neq k_o}^{M_l} \left(\frac{f_{lk}}{f_{lko}}\right)^2 \sum_{n=0}^{L_l-1} |A_{lk} e^{j\psi_{lk}} e^{(\alpha_{lk} + j2\pi f_{lk})nT_{sl}}|^2}{\sum_{k=1}^{M_l} \sum_{n=0}^{L_l-1} |A_{lk} e^{j\psi_{lk}} e^{(\alpha_{lk} + j2\pi f_{lk})nT_{sl}}|^2 + \sum_{v_h \in \Omega_{v_l}} \sum_{k=1}^{M_h} \sum_{n=0}^{L_h-1} |A_{hk} e^{j\psi_{hk}} e^{(\alpha_{hk} + j2\pi f_{hk})nT_{sh}}|^2} \quad (10)$$

$$\Delta STK_h(v_h) = \frac{\sum_{k=1}^{M_h} \left(\frac{f_{hk}}{f_{hko}}\right)^2 \sum_{n=0}^{L_h-1} |A_{hk} e^{j\psi_{hk}} e^{(\alpha_{hk} + j2\pi f_{hk})nT_{sh}}|^2}{R_w \cdot \sum_{k=1}^{M_l} \sum_{n=0}^{L_l-1} |A_{lk} e^{j\psi_{lk}} e^{(\alpha_{lk} + j2\pi f_{lk})nT_{sl}}|^2 + \sum_{k=1}^{M_h} \sum_{n=0}^{L_h-1} |A_{hk} e^{j\psi_{hk}} e^{(\alpha_{hk} + j2\pi f_{hk})nT_{sh}}|^2} \quad (11)$$

Once again, the obtained expressions clearly show how each of the considered ranges of frequencies influences, e.g., global eddy current losses.

Note that the evaluation of the proposed indices is useful for setting limits of emissions and for analyzing the effects on system components of specific waveform distortions at low-frequency and/or at high-frequency. For example, significant ΔSTK_h values reveal a huge presence of spectral content in the high-frequency range; thus, in the presence of electrical machines and transformers, significant eddy currents can be expected in the ferromagnetic core, and should be prevented. In summary, the examination of the proposed index values allows both the characterization of the spectral content included in the analyzed waveform, and the identification of the main problems that can affect the installation in the presence of such distortion.

Obviously, the proposed PQ indices have a time-varying behavior; however, in general, it is required that the PQ indices be numbers able to quantify the levels of PQ disturbances in a synthetic way. Based on this consideration, the evaluation of the mean value or of the 99th or of the 95th percentile over a defined time horizon can be performed for all of the proposed PQ indices. This allows an improvement in the characterization of both low-frequency and high-frequency distortions related to a specific site or installation, and, consequently, the diagnostic role of the proposed indices can also be optimized. Finally, the use of the aforementioned statistical indicators prevents the need to store a

huge amount of data. This encourages the practical application of the proposed indices for long time monitoring, also.

4. Numerical Applications

Several numerical experiments were performed both on synthetic and measured waveforms in different operating conditions of typical generation systems in order to verify the effectiveness of the proposed indices. However, for the sake of brevity, only four case studies are presented in this Section. These case studies are included in two separated Sub-Sections, focusing on renewable generation (case studies 1–3) and modern non-linear loads (case study 4), respectively. In particular, with reference to the renewable generation, the first and second case studies deal with a synthetic waveform and to an actual waveform measured at the PCC of a PVS, respectively. The third case study focuses on the current recorded to the PCC of a PVS in the presence of a simulated short-circuit in the International Council on Large Electric Systems (CIGRE) North American medium voltage (MV) Network Benchmark with a single PVS [24].

The analyses were conducted by means of the SWWMEM presented in [4]. Moreover, a sensitivity analysis was also performed for each case study by considering different lengths of the analysis window for the estimation of high-frequency spectral components. In particular, the evaluation of the proposed PQ indices for the high-frequency range is shown firstly with reference to a very short analysis window (instantaneous approach) and then to a slightly larger analysis window (late approach). (Note that the instantaneous approach is generally faster than the late approach, which can reach significantly higher computational time, as the variability in time and the number of high-frequency spectral components increase).

Moreover, the proposed indices evaluated by means SWWMEM were compared with the indices evaluated by means of STFT and the Prony methods [16,25]. The new indices were also compared with other PQ indices suggested in relevant literature and in the IEC standards [7,12]. These are the group total harmonic distortion (THDG) at low- and at high-frequency, evaluated by means of SWWMEM.

With reference to modern non-linear loads, the aim of the fourth case study is to test the sensitivity of the proposed PQ indices when multiple disturbing sources are connected at the same PCC. Specifically, the fourth case study analyzes, through the instantaneous SWWMEM approach, the actual current waveforms measured at the PCC of a fluorescent lamp installation, when one, ten, and forty-eight lamps are supplied.

All of the waveform analyses were performed in the MATLAB® environment. The MATLAB programs were developed and tested on a Windows PC with an Intel i7-3770 3.4 GHz and 16 GB of RAM. A final discussion on the obtained results is presented in the last Sub-Section.

4.1. Renewable Generation

4.1.1. Case Study 1

A 0.25 s synthetic waveform that emulates the current at the PCC of a PVS is considered. The interface between the PVS and the distribution network is a full-bridge, unipolar inverter, controlled by means of a PWM technique with a frequency modulation index m_f equal to 200. A fundamental component equal to 40 A at 50.02 Hz is also assumed, and, as a background effect, all of the odd harmonics up to the 27th order (low-frequency components) have been included in the synthetic waveform. Finally, a frequency-modulated, high-frequency spectral component and white noise with a standard deviation of 0.001 was also added to the aforesaid components. Figure 2 shows a few milliseconds of the waveform under study. Specifically, Figure 2a shows the time trend of the original waveform, while Figure 2b,c shows the time trend of the low-frequency and high-frequency waveforms obtained by the DWT decomposition, respectively.

A sampling frequency of 10 MHz was chosen; this value is highly sufficient for the detection of all of the spectral components included in the synthetic waveform. In particular, the spectral components

of primary interest are around the order of $2m_f$, in line with the expectations of the hypothesized type of inverter. The amplitude of this group of spectral components was fixed up to 2% of the fundamental, since high-irradiance conditions for the PV system were emulated by means of this synthetic waveform [26].

The frequency-modulated spectral component $s_{tv}(t)$ was a tone at $f_{tv} = 17,598$ Hz with a sinusoidal modulation in frequency, according to Equation (12):

$$s_{tv}(t) = A_{tv} \cos(2\pi f_{tv}t + \varphi_{tv}(t)), \quad (12)$$

where:

$$\varphi_{tv}(t) = A_\varphi \sin(2\pi f_\varphi t), \quad (13)$$

and A_{tv} was fixed equal to 0.5% of the fundamental amplitude, A_φ was 5 Hz and f_φ was 1 Hz. This component emulated secondary emission, commonly detectable at the PCC of distributed generation systems, especially in the high-frequency range.

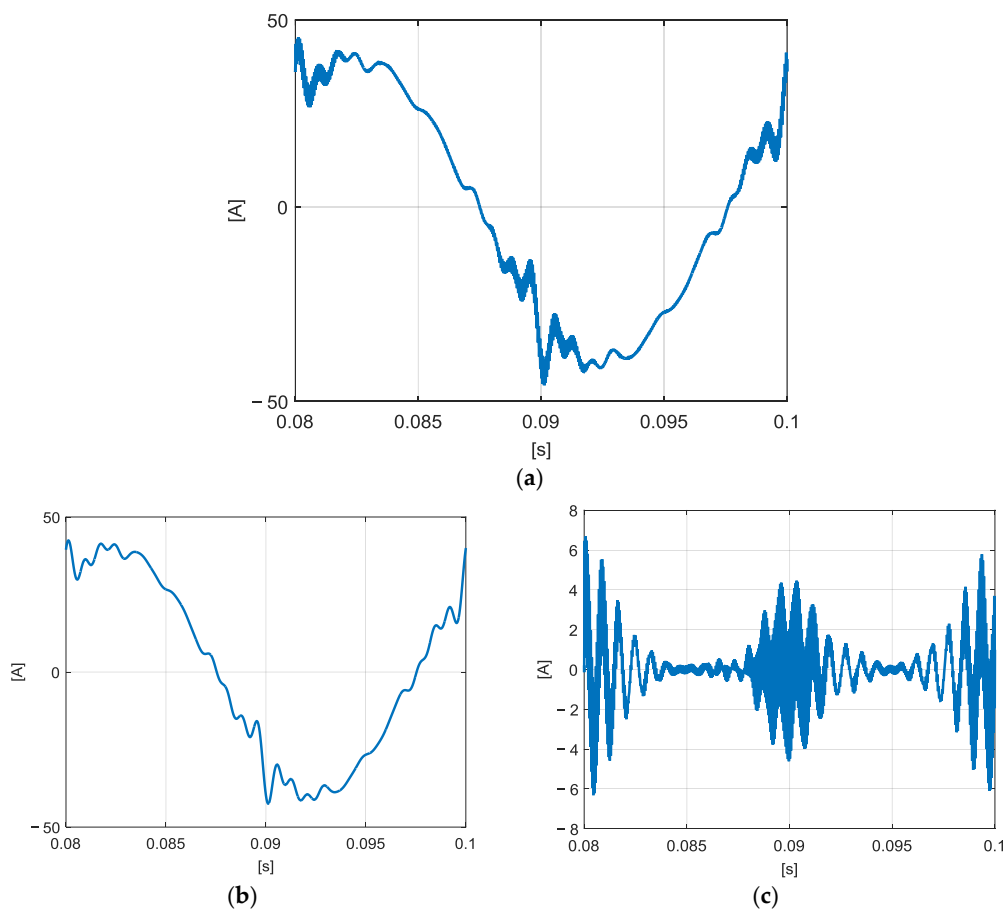


Figure 2. Case study 1: time trend of the waveform under study in terms of (a) original waveform, (b) low-frequency waveform, and (c) high-frequency waveform.

Two different analyses were performed by SWWMEM for the assessment of the waveform distortion of the synthetic waveform under study. For the detection of the low-frequency spectral content, both of the analyses utilized the same duration of time window, i.e., 0.04 s. Thus, the only difference was for the window duration of the spectral analysis in the high-frequency range. Specifically, the first analysis was performed using the instantaneous approach, since it considered a very short analysis window for the detection of the high-frequency spectral content (0.5 ms). Figure 3 shows the

3D representation of the high-frequency spectra obtained by means of the instantaneous SWWMEM approach for the waveforms under test, while Figures 4 and 5 show the results in terms of the proposed indices obtained by this first approach for low-frequency distortions (red line) and high-frequency distortions (blue line).

Specifically, Figure 4 shows the time trend of the instantaneous evaluation of the $STDE_h$ superimposed to the $STDE_l$. It is possible to observe that $STDE_l$ is fixed at 0.105 p.u., while $STDE_h$ varies in time from a minimum of 0.005 p.u. to a maximum of 0.07 p.u. However, $STDE_h$ is always lower than $STDE_l$.

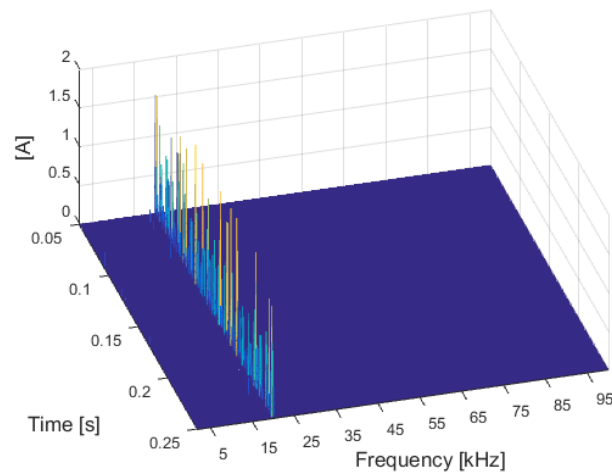


Figure 3. Case study 1: 3D representation of the high-frequency spectra obtained by means of the instantaneous SWWMEM approach.

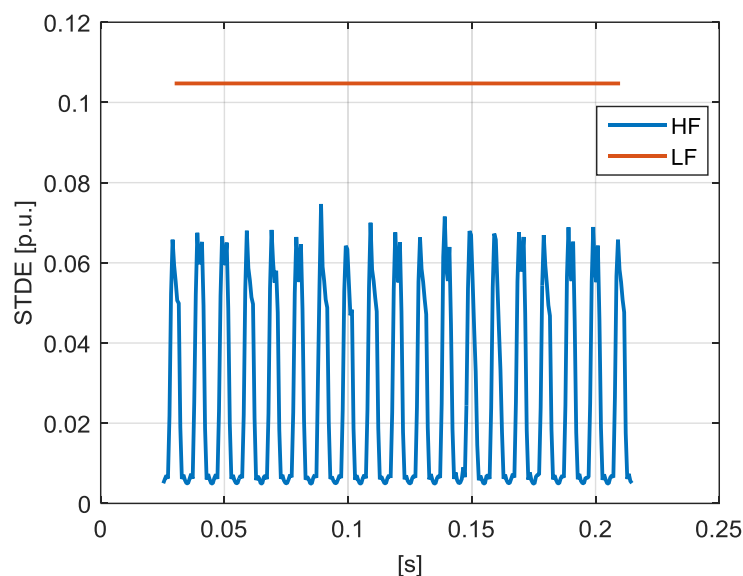


Figure 4. Case study 1: STDE at low-frequency ($0 \div 2$ kHz, red line) and at high-frequency ($2 \div 150$ kHz, blue line) obtained by the instantaneous approach.

Figure 5 shows the time trend of the instantaneous evaluation of the $\Delta STFD_h$ superimposed on the $\Delta STFD_l$. Once again, it is possible to observe that $\Delta STFD_l$ is constant, while $\Delta STFD_h$ varies in time reaching almost 109 Hz. Note that $\Delta STFD_h$ is significantly higher than $\Delta STFD_l$, evidencing, for example, the heavy contribution of the high-frequency distortions to the potential ferromagnetic core losses in electrical machines.

Similar conclusions can also be drawn from an analysis of Figure 6, where the time trends of the instantaneous evaluation of the ΔSTK_h and ΔSTK_l can be observed. It is worth noting that ΔSTK_h reaches almost 880 p.u., while ΔSTK_l is practically negligible, so the main contribution to potential losses based on the squared frequency is made by the high-frequency distortions.

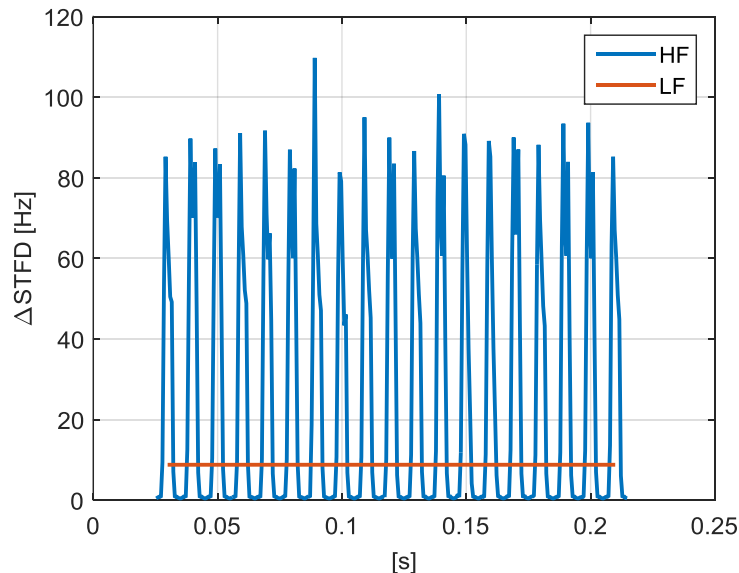


Figure 5. Case study 1: $\Delta STFD$ at low-frequency (0 ÷ 2 kHz, red line) and at high-frequency (2 ÷ 150 kHz, blue line) obtained by the instantaneous approach.

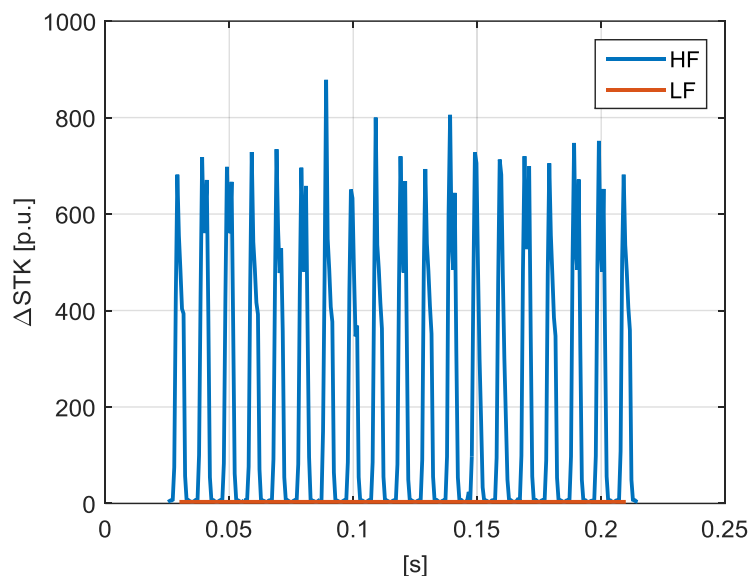


Figure 6. Case study 1: ΔSTK at low-frequency (0 ÷ 2 kHz, red line) and at high-frequency (2 ÷ 150 kHz, blue line) obtained by the instantaneous approach.

The second analysis was based on utilizing a larger analysis window (i.e., 0.01 s) than the previous one for the detection of the high-frequency distortions; the late approach is performed on the proposed indices. Figures 7–9 show the time trends of the proposed indices obtained by this analysis for both low-frequency distortions (red line) and high-frequency distortions (blue line). Note that the time trends of $STDE_l$, $\Delta STFD_l$ and ΔSTK_l are identical to those already observed in Figures 4–6,

respectively, since the low-frequency analyses were performed using the same window duration for both the instantaneous and late approach. They are included in Figures 7–9 to facilitate comparison.

The late approach shows, for the high-frequency distortions, an almost constant trend for all of the proposed indices. In particular, the values of the proposed high-frequency indices in Figures 7–9 approach the mean values of the corresponding time trends in Figures 4–6. Their values are: (i) 0.037 p.u. for $STDE_{hi}$; (ii) 26 Hz for $\Delta STFD_{hi}$; (iii) 210 p.u. for ΔSTK_{hi} .

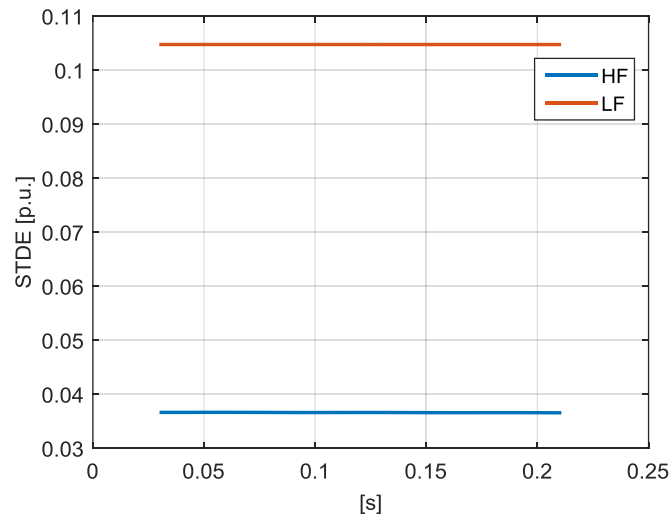


Figure 7. Case study 1: STDE at low-frequency (0 ÷ 2 kHz, red line) and at high-frequency (2 ÷ 150 kHz, blue line) obtained by the late approach.

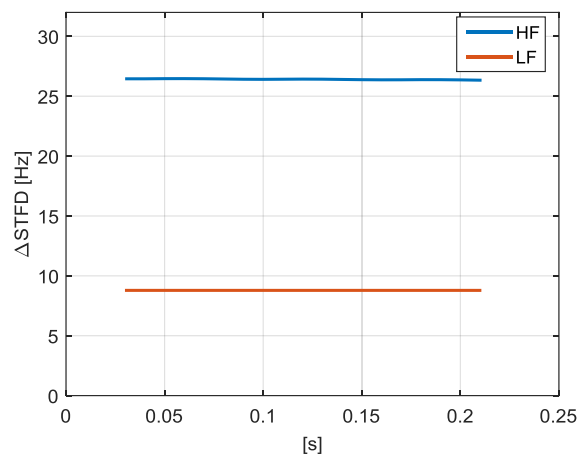


Figure 8. Case study 1: $\Delta STFD$ at low-frequency (0 ÷ 2 kHz, red line) and at high-frequency (2 ÷ 150 kHz, blue line) obtained by the late approach.

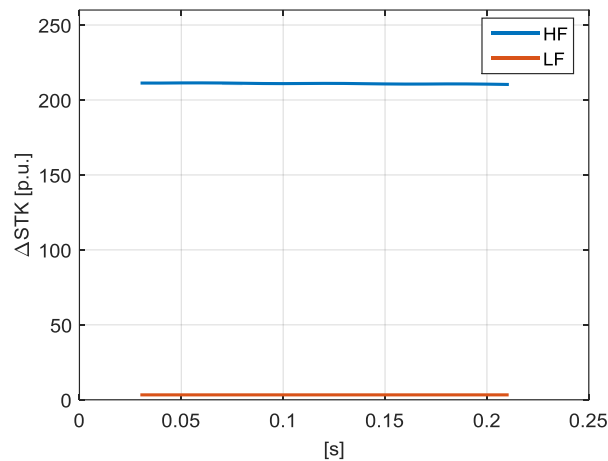


Figure 9. Case study 1: ΔSTK at low-frequency ($0 \div 2$ kHz, red line) and at high-frequency ($2 \div 150$ kHz, blue line) obtained by the late approach.

Finally, it is easy to observe that the late approach also confirms the dominant role of high-frequency distortions in comparison to low-frequency distortions in the proposed indices presented in Figures 8 and 9, while $STDE_h$ in Figure 7 proves to have a lower, although comparable, value than $STDE_l$, evidencing the fact that both the considered low-frequency and high-frequency disturbances contribute equally to potential problems related to the overheating of electrical devices.

4.1.2. Case Study 2

A 0.2 s measured current window was recorded at the PCC of a single-phase, 2.5 kW PV, and analyzed by means of SWWMEM. The measurement was performed with a Hioki, model 8855 instrument. The sampling of the current was performed at 10 MS/s and with 12-bit amplitude resolution. A 1st order low-pass filter with a cut-off frequency of 1 MHz was used for anti-aliasing purposes. The current was picked up by a Pearson current model 411 probe which is a permanently closed model. This current probe has a transfer of 100 mV/A and the lower 3 dB cutoff is at 5 Hz and the high cutoff at 20 MHz. In the frequency range of interest the accuracy is $-0, +1\%$ dB and the phase error of the probe is less than 1 degree from 300 Hz to 33.3 kHz and increasing to 6 degrees at 2 MHz. The probe can handle up to 40 Ampere at 50 Hz. Figure 10 shows a few milliseconds of the waveform under study. Specifically, Figure 9a shows the time trend of the original waveform, while Figure 10b,c shows the time trend of the low-frequency and high-frequency waveforms obtained by the DWT decomposition, respectively. The sampling rate was 10 MHz, so a proper detection of both low-frequency and high-frequency spectral components was possible.

Additionally, in this case study, the two different approaches described above were applied and, obviously, once again, both of them utilized the same duration of time window—i.e., 0.04 s—for the analysis of the low-frequency waveform. Their only difference is for the spectral analysis of the high-frequency waveform. Specifically, Figure 11 shows the 3D representation of the high-frequency spectra obtained by means the instantaneous SWWMEM approach for the waveforms under test. This instantaneous approach, with a very short analysis window for the detection of the high-frequency spectral content (0.5 ms), provides the results shown in Figures 12–14 for the proposed indices.

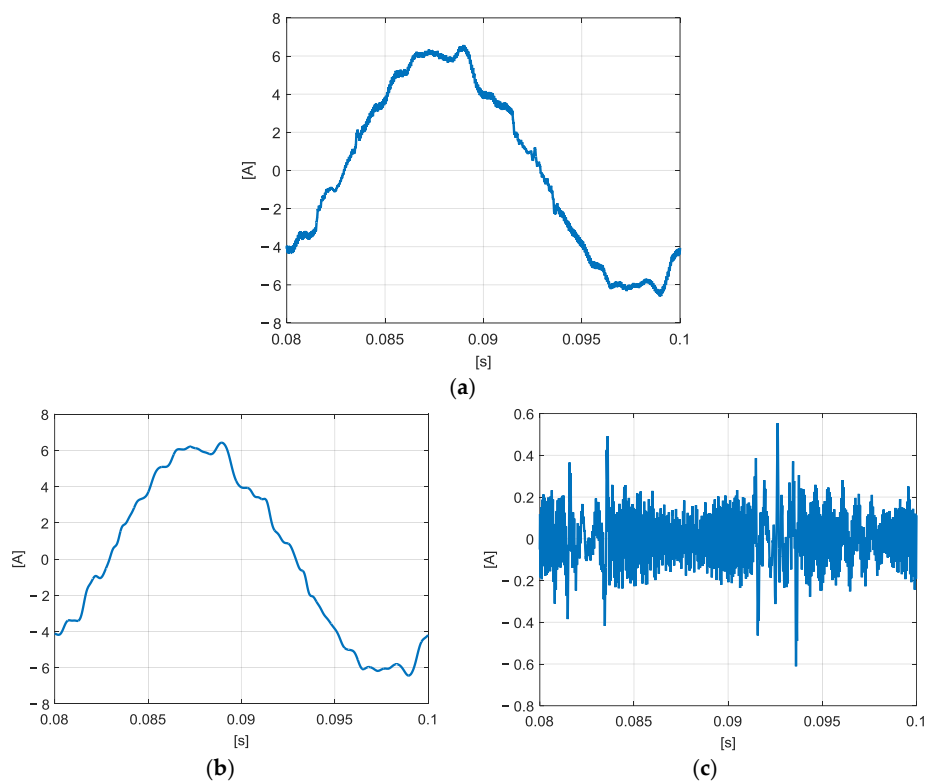


Figure 10. Case study 2: time trend of the waveform under study in terms of (a) original waveform, (b) low-frequency waveform and (c) high-frequency waveform.

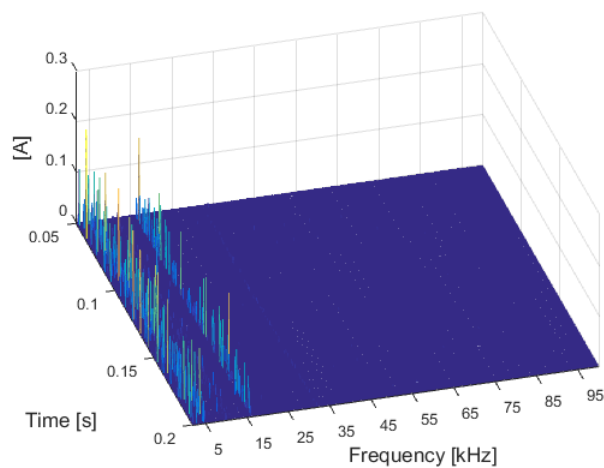


Figure 11. Case study 1: 3D representation of the high-frequency spectra obtained by means the instantaneous approach of SWWMEM.

Figure 12 shows a time trend of the $STDE_l$ ($0 \div 2$ kHz, red line) that is almost constant around 0.075 p.u., and a time trend of the $STDE_h$ (blue line) that is significantly variable from 0.01 p.u. to 0.06 p.u. Similarly, a practically constant $\Delta STFD_l$ (red line) and a variable $\Delta STFD_h$ (blue line) can be observed in Figure 11, with values of $\Delta STFD_h$ generally significantly higher than $\Delta STFD_l$ in time. Finally, Figure 13 shows a negligible ΔSTK_l (red line) and a very high ΔSTK_h (blue line) that reaches 300 p.u. Hence, Figures 12–14 confirm, in an actual case, the behavior of both low-frequency and high-frequency distortions already observed in the previous theoretical case study, proving that the two frequency ranges can contribute equally to problems relating to the overheating of electrical

components included in a PVS installation. Conversely, the problems related to the ferromagnetic core losses in electrical machines potentially included in the considered installation could only be due to the presence of high-frequency distortions.

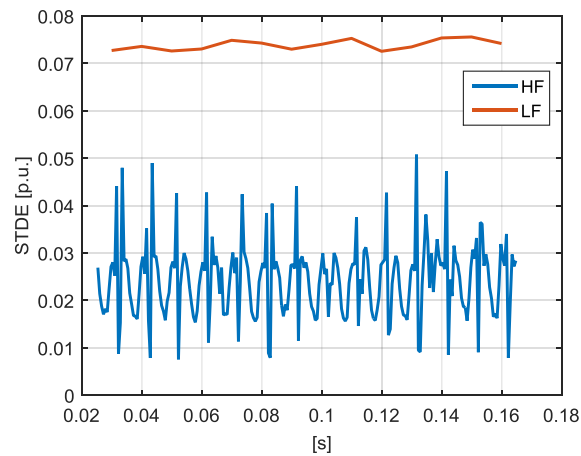


Figure 12. Case study 2: STDE at low-frequency ($0 \div 2$ kHz, red line) and at high-frequency ($2 \div 150$ kHz, blue line) obtained by the instantaneous approach.

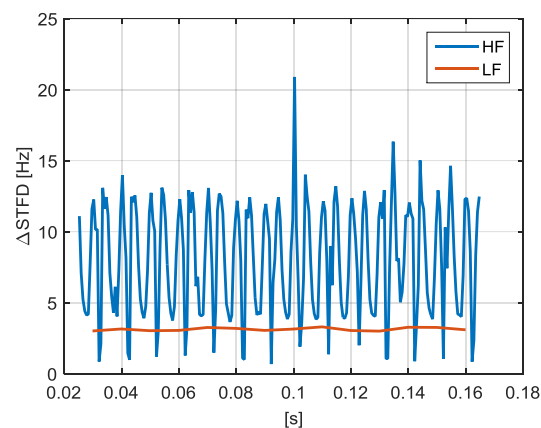


Figure 13. Case study 2: $\Delta STFD$ at low-frequency ($0 \div 2$ kHz, red line) and at high-frequency ($2 \div 150$ kHz, blue line) obtained by the instantaneous approach.

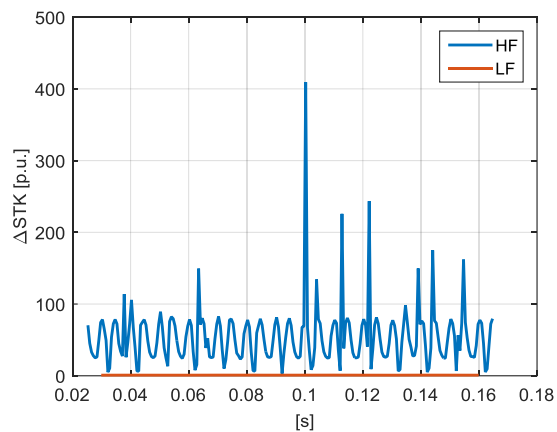


Figure 14. Case study 2: ΔSTK at low-frequency ($0 \div 2$ kHz, red line) and at high-frequency ($2 \div 150$ kHz, blue line) obtained by the instantaneous approach.

The second approach, as previously stated, is based on the use of a larger analysis window for the high-frequency detection (i.e., 0.01 s). The corresponding results in terms of proposed indices are shown in Figures 15–17.

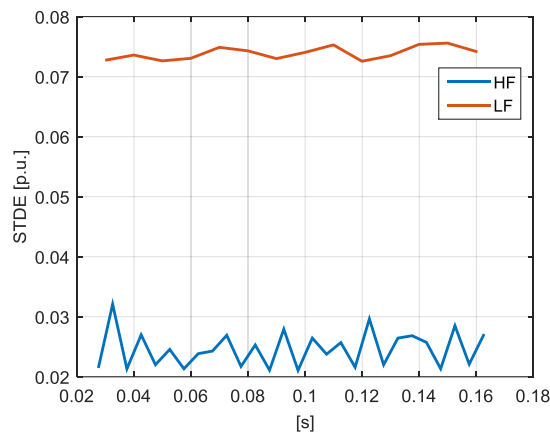


Figure 15. Case study 2: STDE at low-frequency (0 ÷ 2 kHz, red line) and at high-frequency (2 ÷ 150 kHz, blue line) obtained by the late approach.

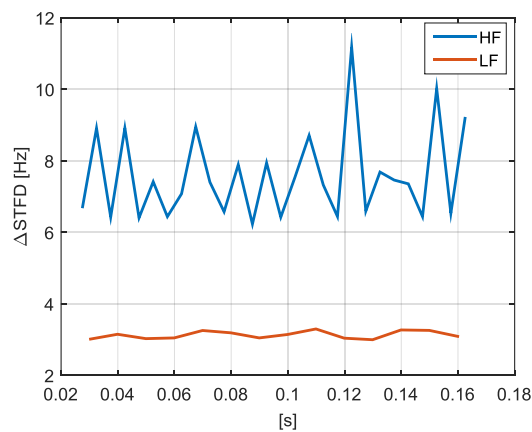


Figure 16. Case study 2: ΔSTFD at low-frequency (0 ÷ 2 kHz, red line) and at high-frequency (2 ÷ 150 kHz, blue line) obtained by the late approach.

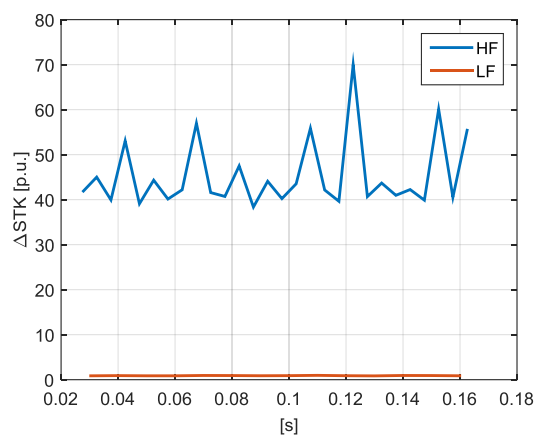


Figure 17. Case study 2: ΔSTK at low-frequency (0 ÷ 2 kHz, red line) and at high-frequency (2 ÷ 150 kHz, blue line) obtained by the late approach.

Note that the time trends of $STDE_l$, $\Delta STFD_l$ and ΔSTK_l (red lines) are those already observed in Figures 12–14, and they are included in Figures 15–17 only to facilitate comparison. Otherwise, the time trends of $STDE_h$, $\Delta STFD_h$ and ΔSTK_h (blue lines) in Figures 15–17 change significantly, presenting slower and more restrained variations than in Figures 12–14 due to the longer duration of the analysis window. However, the mean values of $STDE_h$, $\Delta STFD_h$ and ΔSTK_h in Figures 15–17 are analogous to those in Figures 12–14, respectively, so, once again, the role of the high-frequency disturbances has to be considered predominant as a possible cause of detrimental effects.

4.1.3. Case Study 3

A 0.2 s current waveform was obtained by simulating in PSCAD a short-circuit at a bus of the CIGRE North American MV Network Benchmark with a single PVS, as described in [19,24]. This is a 60 Hz system, operating at 12.47 kV, and it is commonly utilized as a reference tool for distributed energy resource integration. The transient currents are measured at PCC of the PVS and refer to the effect of a short-circuit at bus #6 of the network. Note that the PVS, allocated to bus #3, is also connected to the network after the fault. Figure 18 shows a few milliseconds of the waveform under study. Specifically, Figure 18a shows the time trend of the original waveform, while Figure 18b,c show the time trend of the low-frequency and high-frequency waveforms obtained by the DWT decomposition, respectively. The sampling rate was 50 kHz, so proper detection of high-frequency spectral components up to 25 kHz was possible.

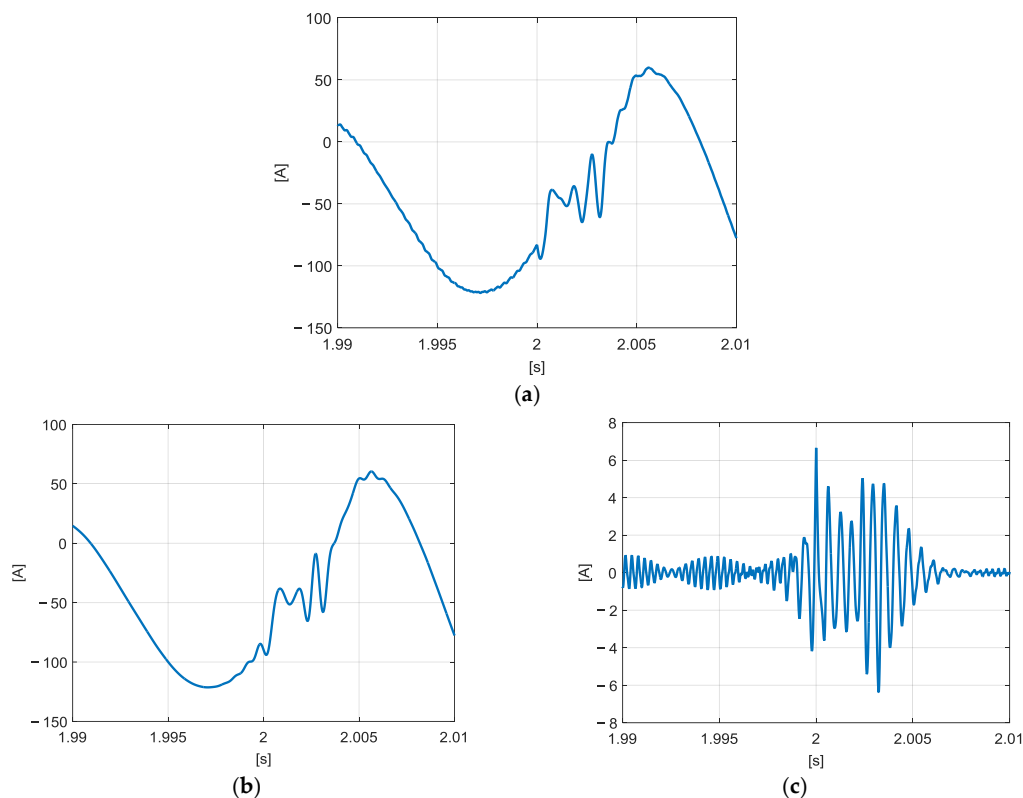


Figure 18. Case study 3: time trends of the waveform under study in terms of (a) original waveform, (b) low-frequency waveform and (c) high-frequency waveform.

The two approaches described above were also applied in this last case study. Specifically, the instantaneous approach, considering a very short analysis window for the detection of the high-frequency spectral content (0.16 ms), provided the results shown in Figures 19–21 in terms of the proposed indices.

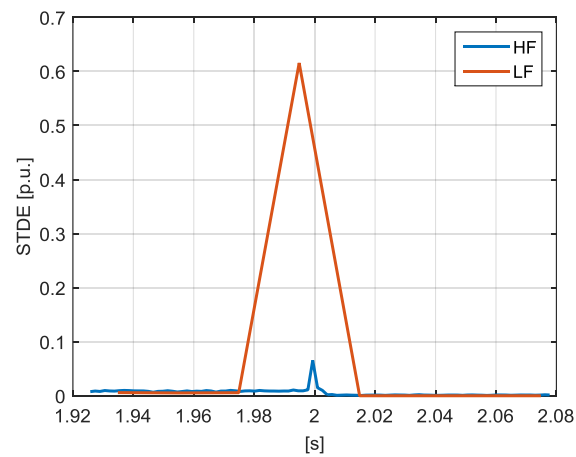


Figure 19. Case study 3: STDE at low-frequency ($0 \div 2.4$ kHz, red line) and at high-frequency ($2.4 \div 150$ kHz, blue line) obtained through the instantaneous approach.

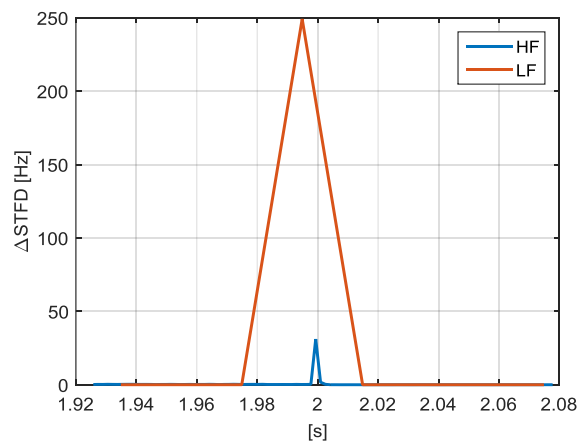


Figure 20. Case study 3: $\Delta STFD$ at low-frequency ($0 \div 2.4$ kHz, red line) and at high-frequency ($2.4 \div 150$ kHz, blue line) obtained through the instantaneous approach.

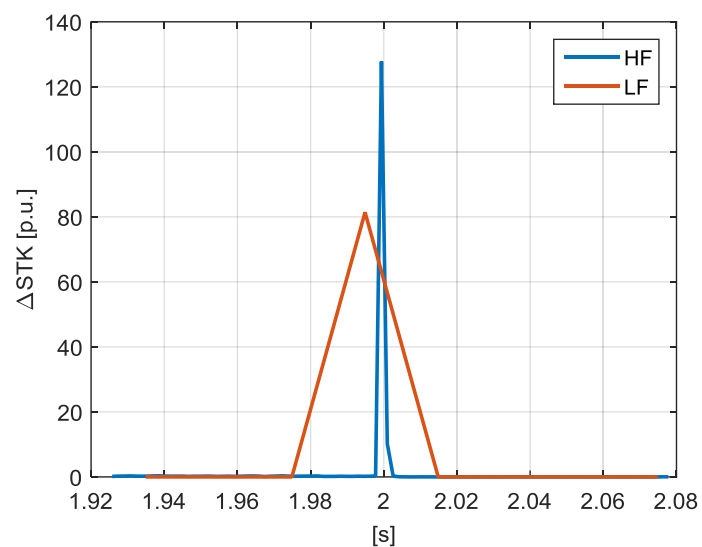


Figure 21. Case study 3: ΔSTK at low-frequency ($0 \div 2.4$ kHz, red line) and at high-frequency ($2.4 \div 150$ kHz, blue line) obtained through the instantaneous approach.

Figures 19–21 show time trends for all of the proposed indices; they are significantly different compared to those obtained in the previous two case studies. In particular, all of the proposed PQ indices clearly provide the localization of the transient, with an impulsive behavior around 2 s, and piecewise constant trends otherwise, both for the low-frequency range (for which the transient is detected from 1.975 s to 2.015 s) and for the high-frequency range (for which the transient is detected from 1.998 s to 2.004 s). Note that high-frequency indices provide better localization in time for the transient than the low-frequency indices, as a result of the different durations of the analysis windows chosen for the two considered frequency ranges. Moreover:

Figure 19 shows for $STDE_l$ (red line) a peak value equal to 0.62 p.u. corresponding to the transient, while for $STDE_h$ (blue line) the peak value of the transient is equal to 0.065 p.u.;

Figure 20 shows for $\Delta STFD_l$ (red line) a peak value equal to 249.10 Hz corresponding to the transient, while for $\Delta STFD_h$ (blue line) the peak value of the transient is equal to 31.10 Hz;

Figure 21 shows for ΔSTK_l (red line) a peak value equal to 81.40 p.u. corresponding to the transient, while for ΔSTK_h (blue line) the peak value of the transient is equal to 127.80 p.u.

The previous observations indicate that only the ΔSTK indices provide higher values at high-frequency than at low-frequency, while the other proposed indices are characterized by a predominance of the low-frequency curve over the high-frequency curve. This result indicates that the transient is characterized by spectral components at high-frequency with low amplitudes, and is confined to a very small range, which does not exceed 25 kHz. These values for high-frequencies, characterized by $STDE_h < 0.1$ p.u., determine that $\Delta STFD_h < \Delta STFD_l$. However, the squared normalized frequency in the definition of ΔSTK_h allows, once again, $\Delta STK_h > \Delta STK_l$.

With reference to the steady-state conditions before and after the transient, the values of the indices are always greater before the fault due to a reduced value of the fundamental current, although this is not clearly visible in Figures 19–21.

Now, let us consider the late approach, which, as previously specified, is based on the use of a larger analysis window for high-frequency detection (i.e., 0.01 s). The corresponding results in terms of the proposed indices are shown in Figures 22–24.

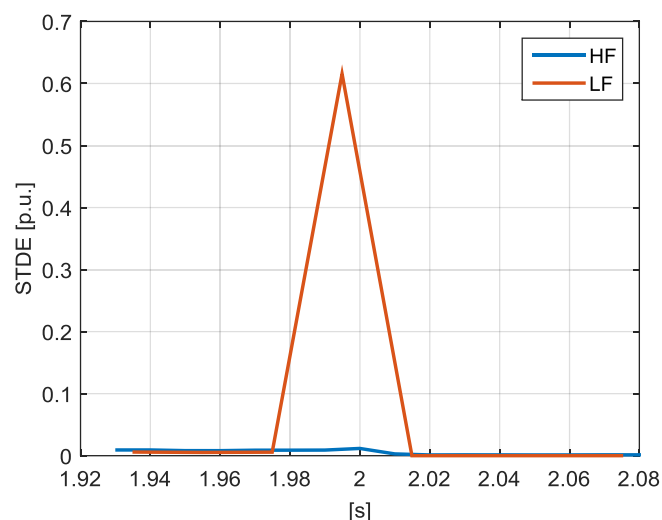


Figure 22. Case study 3: STDE at low-frequency ($0 \div 2.4$ kHz, red line) and at high-frequency ($2.4 \div 150$ kHz, blue line) obtained through the late approach.

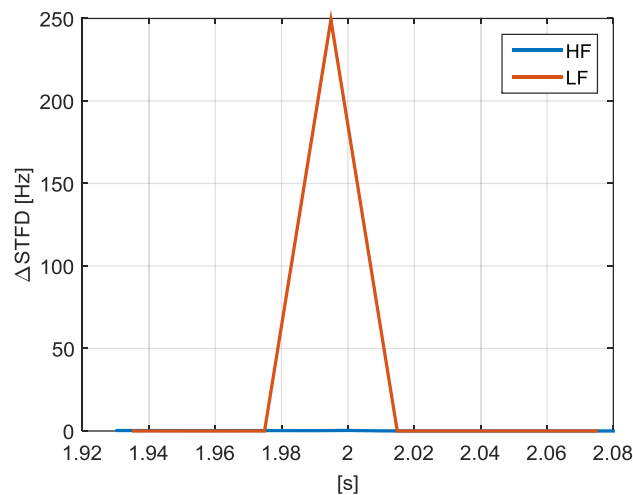


Figure 23. Case study 3: $\Delta STFD$ at low-frequency ($0 \div 2.4$ kHz, red line) and at high-frequency ($2.4 \div 150$ kHz, blue line) obtained through the late approach.

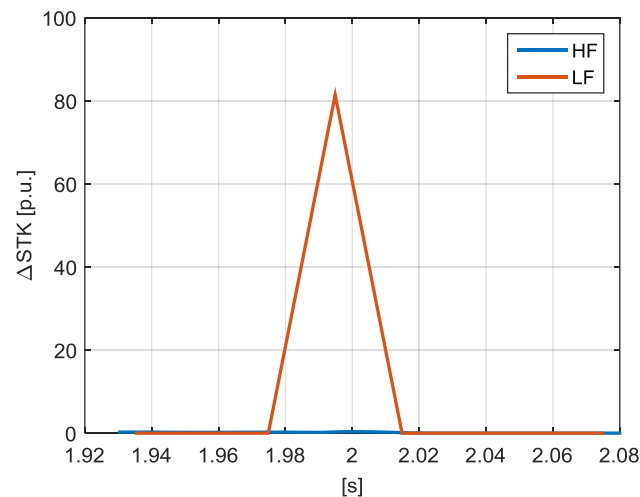


Figure 24. Case study 3: ΔSTK at low-frequency ($0 \div 2.4$ kHz, red line) and at high-frequency ($2.4 \div 150$ kHz, blue line) obtained through the late approach.

Figures 22–24 show for $STDE_l$, $\Delta STFD_l$ and ΔSTK_l (red lines) the same time trends observable in Figures 19–21, while the time behavior of $STDE_h$, $\Delta STFD_h$ and ΔSTK_h (blue lines) is clearly different from those obtained by means of the instantaneous approach. Specifically, the late approach, managing small amplitudes over larger time intervals, spreads the transient high-frequency spectral content in the time-window, hiding its presence. The above considerations involve the fact that transient detection necessarily requires the use of a very small window for the analysis of the high-frequency range.

4.1.4. Proposed Indices Evaluated by Other Methods

The evaluation of the proposed indices was also performed by analysing the waveforms of the previous case studies through STFT and Prony's methods. Both methods prevent the separate evaluation of the low-frequency and the high-frequency components, so only a late approach was performed, utilizing window lengths equal to two cycles of the power system frequency. Specifically, a duration of the analysis window equal to 0.04 s was utilized for the first two case studies (50 Hz systems), while a duration of analysis window equal to 0.034 s was utilized for the last case study (60 Hz system).

With reference to the first case study, Figures 25–27 show the results obtained through STFT, while Figures 28–30 provide the results obtained through Prony’s method.

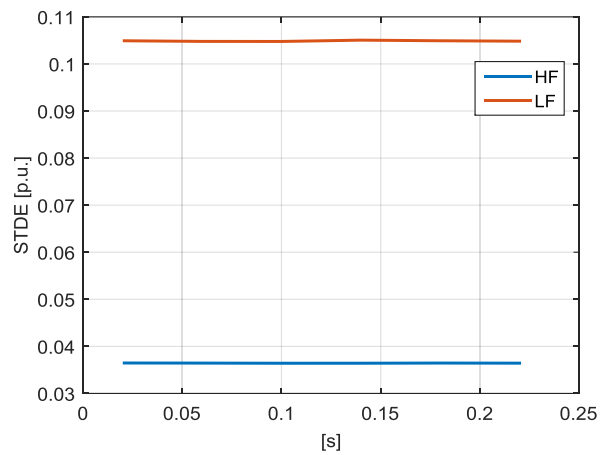


Figure 25. Case study 1: STDE at low-frequency (0 ÷ 2 kHz, red line) and at high-frequency (2 ÷ 150 kHz, blue line) obtained through STFT.

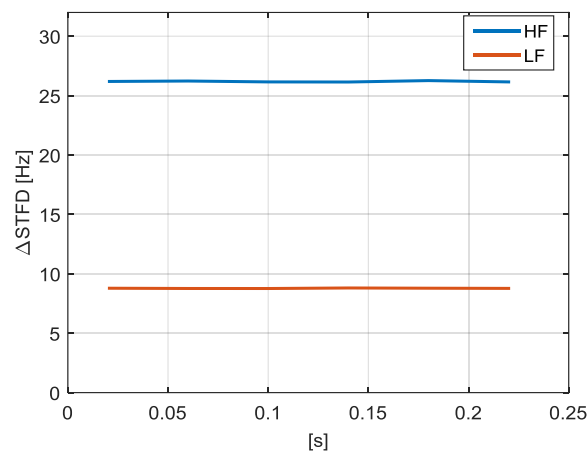


Figure 26. Case study 1: $\Delta STFD$ at low-frequency (0 ÷ 2 kHz, red line) and at high-frequency (2 ÷ 150 kHz, blue line) obtained through STFT.

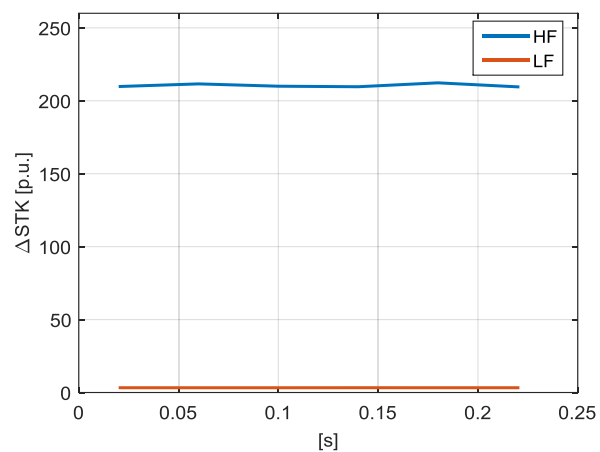


Figure 27. Case study 1: ΔSTK at low-frequency (0 ÷ 2 kHz, red line) and at high-frequency (2 ÷ 150 kHz, blue line) obtained through STFT.

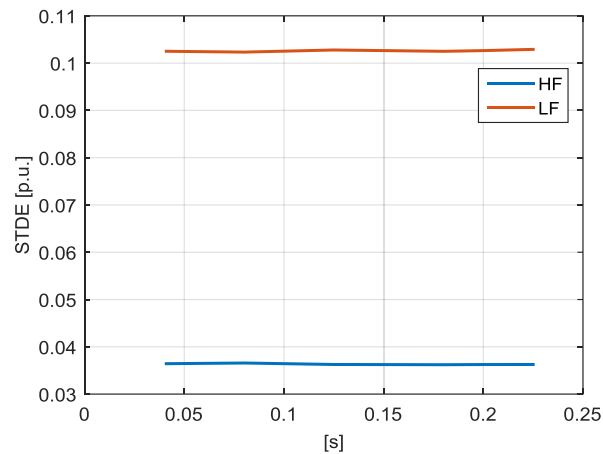


Figure 28. Case study 1: STDE at low-frequency (0 ÷ 2 kHz, red line) and at high-frequency (2 ÷ 150 kHz, blue line) obtained through Prony's method.

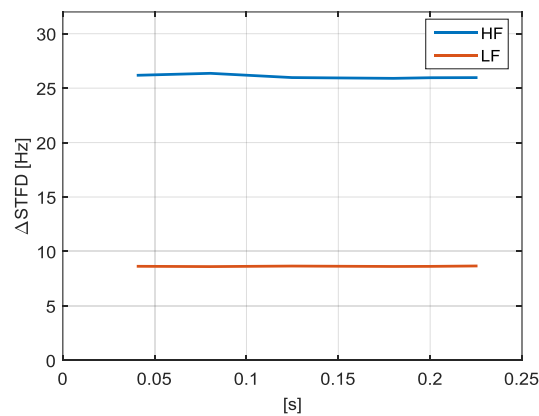


Figure 29. Case study 1: $\Delta STFD$ at low-frequency (0 ÷ 2 kHz, red line) and at high-frequency (2 ÷ 150 kHz, blue line) obtained through Prony's method.

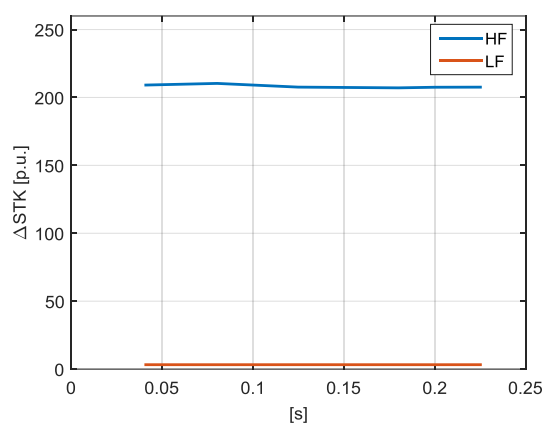


Figure 30. Case study 1: ΔSTK at low-frequency (0 ÷ 2 kHz, red line) and at high-frequency (2 ÷ 150 kHz, blue line) obtained through Prony's method.

The time trends evaluated by using STFT and Prony methods approximate the results obtained by utilizing the late SWWEM approach, presented in Figures 7–9. Therefore, only averaged information about the proposed indices can be obtained by using STFT and Prony methods, preventing the

individuation of any instantaneous variations. Thus, they are not applicable for general purposes, because the obtained results can hide the real severity and the presence of high-frequency spectral components.

Similarly, with reference to the waveform in case study 2, Figures 31–33 show the results obtained through STFT, while Figures 34–36 provide the results obtained through Prony’s method.

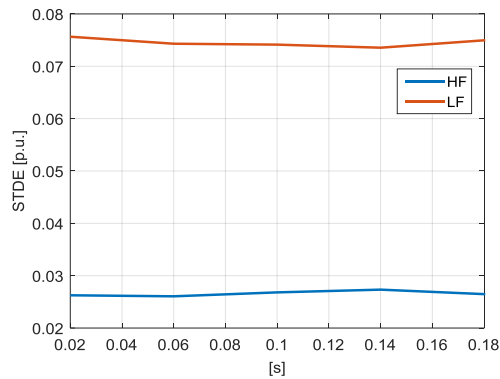


Figure 31. Case study 2: STDE at low-frequency ($0 \div 2$ kHz, red line) and at high-frequency ($2 \div 150$ kHz, blue line) obtained through STFT.

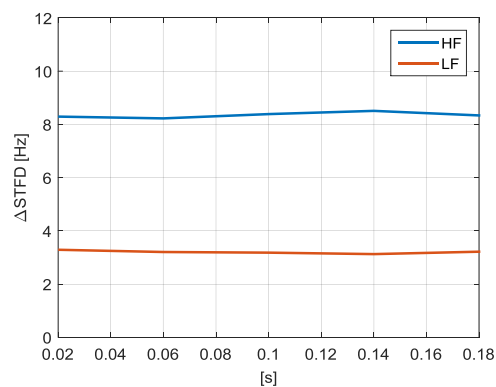


Figure 32. Case study 2: $\Delta STFD$ at low-frequency ($0 \div 2$ kHz, red line) and at high-frequency ($2 \div 150$ kHz, blue line) obtained through STFT.

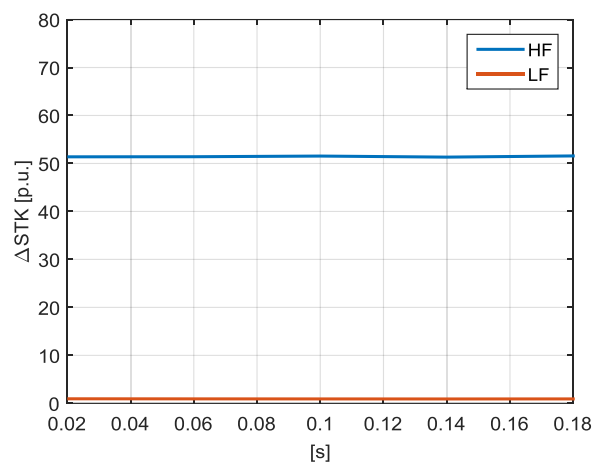


Figure 33. Case study 2: ΔSTK at low-frequency ($0 \div 2$ kHz, red line) and at high-frequency ($2 \div 150$ kHz, blue line) obtained through STFT.

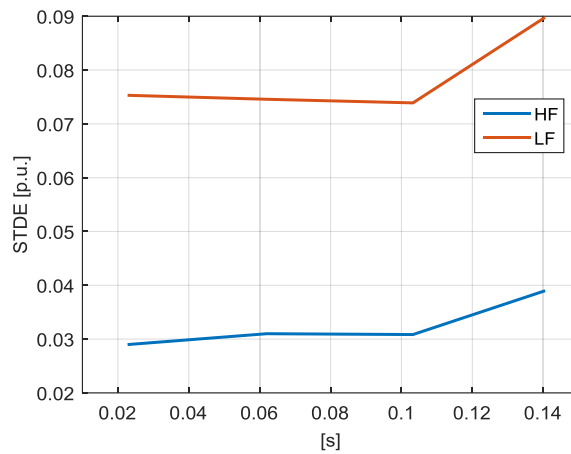


Figure 34. Case study 2: STDE at low-frequency (0 ÷ 2 kHz, red line) and at high-frequency (2 ÷ 150 kHz, blue line) obtained through Prony’s method.

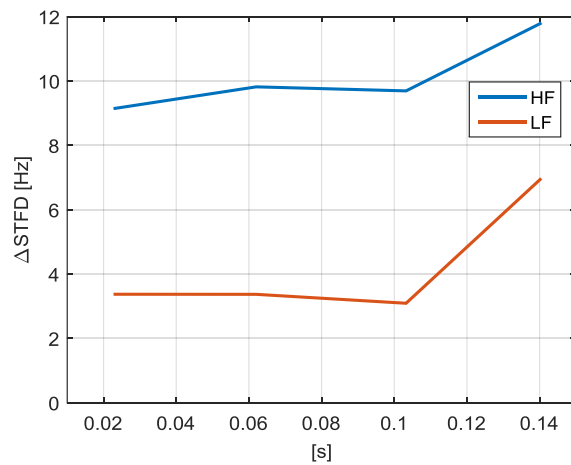


Figure 35. Case study 2: ΔSTFD at low-frequency (0 ÷ 2 kHz, red line) and at high-frequency (2 ÷ 150 kHz, blue line) obtained through Prony’s method.

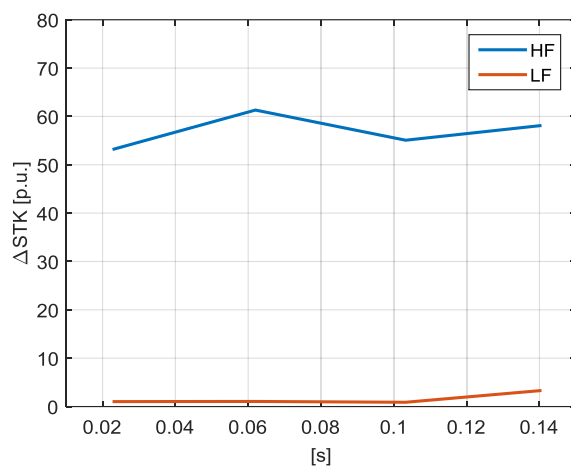


Figure 36. Case study 2: ΔSTK at low-frequency (0 ÷ 2 kHz, red line) and at high-frequency (2 ÷ 150 kHz, blue line) obtained through Prony’s method.

The proposed indices evaluated using STFT and Prony methods only weakly approximate the results obtained by the late SWWMEM approach, presented in Figures 15–17. In particular, while STFT results show a constant behavior corresponding to the averaged values of the results obtained by the late approach with SWWMEM, the results of Prony’s method in the last sliding window significantly deviate from the time trends shown in Figures 15–17. The above outcomes are due to different aspects that characterize or afflict the STFT and Prony’s method. With reference to STFT, the desynchronization between spectral component periods and duration of the analysis window determines spectral leakage problems. These problems are not expected to be particularly significant for the STDE evaluation, since the only differences are the underestimation of the fundamental component and the spread around 2 kHz that determines the spectral content migration from the low- to the high-frequency range (or vice versa). Instead, the spectral leakage should cause deformations in the time trends for the other two types of proposed PQ indices, due to the amplitude reduction of the effective spectral components and the occurrence of non-zero spectral components around them. This phenomenon could produce variations when the frequency (normalized squared frequency) is multiplied by the corresponding spectral component energy in the evaluation of $\Delta STFD$ (ΔSTK). However, since these proposed indices are the weighted sum of the energy of each component with respect to the global energy of the waveform, in many cases the aforesaid variation proves to be attenuated.

With reference to Prony’s method, the main issues are: (i) the huge amount of samples in each analysis window, due to the high sample rate, and the impossibility of separating the total spectral content in low and high-frequency range; this determines convergence problems when the proper combination of complex exponentials has to be found; (ii) the use of window durations equal to a multiple of the fundamental period prevents a proper detection of the high-frequency components.

These difficulties in both STFT and Prony’s method make the use of STFT and Prony’s method inadvisable, and not reliable in the estimation of the proposed PQ indices for wide-spectrum waveforms. In any case, Prony’s method could also be utilized after the decomposition of the spectrum performed by the DWT, reaching analogous performances to SWWMEM.

Finally, with reference to the transient waveform in case study 3, Figures 37–39 show the results obtained through STFT, while Figures 40–42 provide the results obtained through Prony’s method.

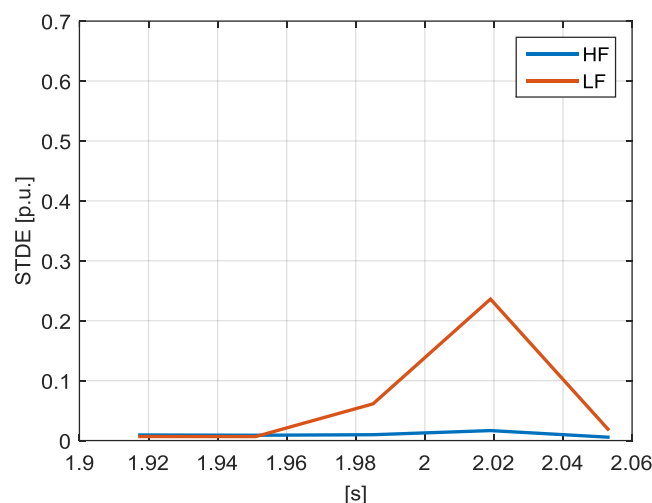


Figure 37. Case study 3: STDE at low-frequency (0 ÷ 2.4 kHz, red line) and at high-frequency (2.4 ÷ 150 kHz, blue line) obtained through STFT.

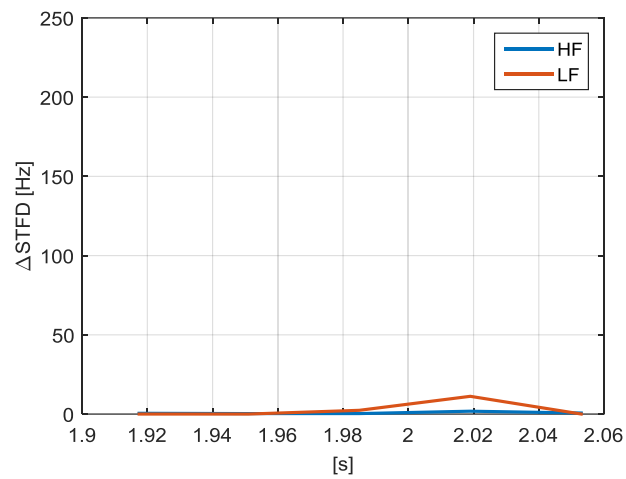


Figure 38. Case study 3: $\Delta STFD$ at low-frequency (0 ÷ 2.4 kHz, red line) and at high-frequency (2.4 ÷ 150 kHz, blue line) obtained through STFT.

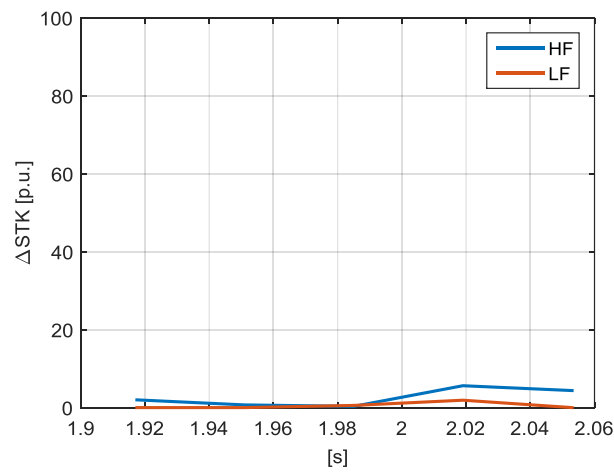


Figure 39. Case study 3: ΔSTK at low-frequency (0 ÷ 2.4 kHz, red line) and at high-frequency (2.4 ÷ 150 kHz, blue line) obtained through STFT.

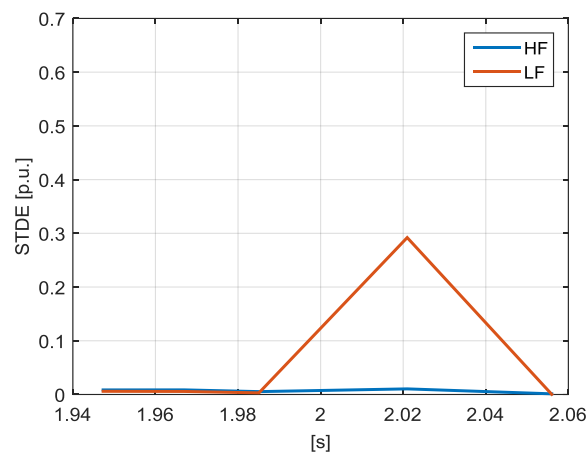


Figure 40. Case study 3: STDE at low-frequency (0 ÷ 2.4 kHz, red line) and at high-frequency (2.4 ÷ 150 kHz, blue line) obtained through Prony's method.

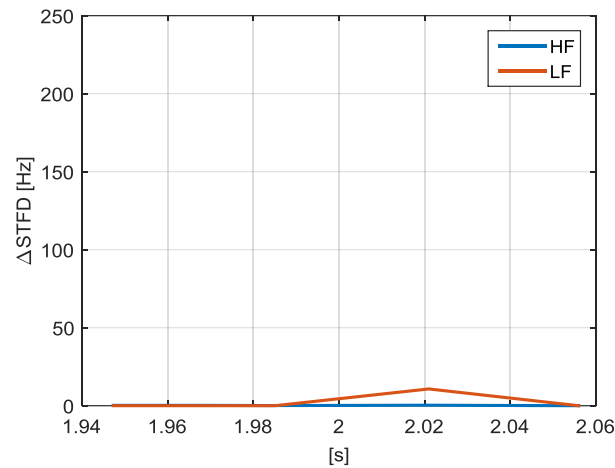


Figure 41. Case study 3: $\Delta STFD$ at low-frequency ($0 \div 2.4$ kHz, red line) and at high-frequency ($2.4 \div 150$ kHz, blue line) obtained through Prony's method.

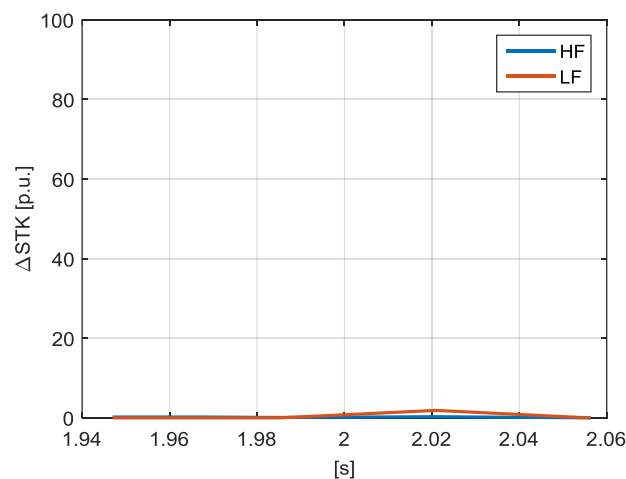


Figure 42. Case study 3: ΔSTK at low-frequency ($0 \div 2.4$ kHz, red line) and at high-frequency ($2.4 \div 150$ kHz, blue line) obtained through Prony's method.

As observed in Figures 37–42, the time trends of the proposed indices evaluated by means of STFT and Prony's method prove to be highly inadequate in this case. In fact, although the time trends of the low-frequency indices provide variations of 2 s, they are very low and the transient presence could be easily hidden in the presence of a more distorted waveform. Moreover, the high-frequency indices assume strangely-negligible values, especially with the Prony's analysis, confirming improper detection of the high-frequency range when all of the wide spectrum is detected in the same analysis.

All of the aforesaid results confirm the need to evaluate the proposed PQ indices by means of SWWMEM, which is currently the only spectral analysis method that specifically addresses the wide-spectrum waveform, as it is properly adapted to both the low- and the high-frequency range.

4.1.5. Comparison with Other Power Quality Indices Available in Literature

In order to provide a comparison of the proposed indices with other PQ indices available in relevant literature [12], THDGs at low- ($THDG_l$) and high-frequency ($THDG_h$) were also evaluated by the same means as the analyses performed through SWWMEM for each of the three case studies.

Note that, although the aim of the THDGs is very similar to the aim of STDEs, many differences exist between STDE and THDG (both at low- and high-frequency). These are:

$STDE_l$ and $STDE_h$ consider the energy of all of the spectral components in the spectrum, while $THDG_l$ and $THDG_h$ utilize the grouping of several harmonic orders, which do not include subharmonic and DC component information;

the fundamental group at the denominators of $THDG_l$ and $THDG_h$ includes all of the spectral components from 25 Hz to 75 Hz, while $STDE_l$ and $STDE_h$ only consider the energy of the fundamental component;

differently from $STDE_l$ and $STDE_h$, there is not a total separation between the numerators of $THDG_l$ and $THDG_h$, since, according to IEC standard [7], the last grouping of the low-frequency range and the first grouping of the high-frequency range have an overlap of 20 Hz.

While $STDE_l$ and $STDE_h$ univocally take into account the presence of damping factors in the ESPRIT model, the grouping definition presents arbitrariness in how to include the information provided by the damping factors; as is well known, they are able to significantly vary the spectral component amplitude along the analysis window. In this paper, the aforesaid influence in the THDG evaluation is taken into account by multiplying the root mean squared (RMS) of the spectral component amplitudes for the damping factor contribution corresponding to the midpoint of any analysis window. However, the inability to include the continuously damped amplitudes in the definition of both $THDG_l$ and $THDG_h$ determines the presence of spikes in the time trends of these two indices.

Figure 43 shows the time trends of THDG at low- (red line) and at high-frequency (blue line) evaluated for the waveform of case study 1, using the same time windows utilized in the instantaneous approach.

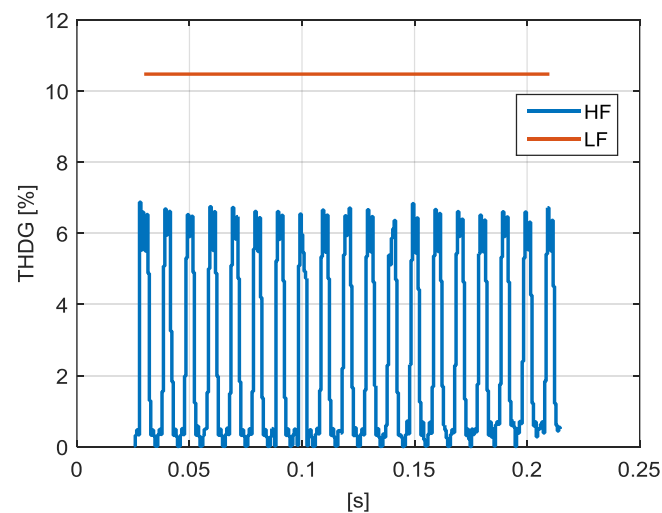


Figure 43. Case study 1: THDG at low-frequency (0 ÷ 2 kHz, red line) and at high-frequency (2 ÷ 150 kHz, blue line).

Figure 43 shows values very similar to the ones in Figure 4 (in %), in line with the aims of both indices. In fact, in this particular case study, the differences previously highlighted between the THDGs and STDEs are smoothed due to the absence of DC and subharmonic components, of interharmonic close to the fundamental component, and of spectral components near 2 kHz. Moreover, the synthetic waveform is easy and perfectly fitted by the ESPRIT model, due to the finite number of spectral components, so the damping factors are generally close to 0, avoiding significant variations of the spectral component amplitudes along the window and consequently limiting the presence of spikes.

Similarly, Figure 44 shows the time trends of THDG at low- and at high-frequency evaluated for the waveform of case study 2 by means SWWMEM, using once again the same time windows utilized in the instantaneous approach.

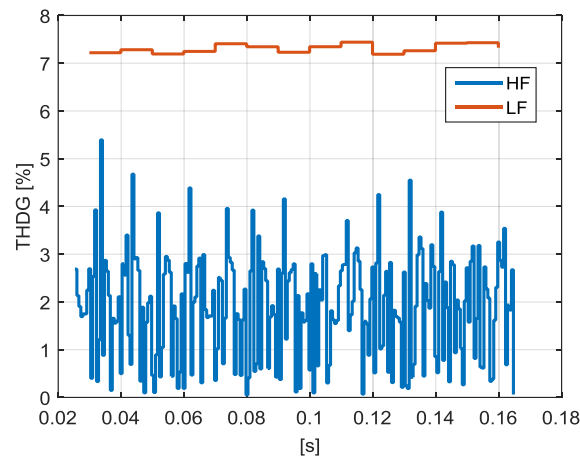


Figure 44. Case study 2: THDG at low-frequency ($0 \div 2$ kHz, red line) and at high-frequency ($2 \div 150$ kHz, blue line).

In this case, the time trend of the $THDG_l$ (red line in Figure 44) is very similar to the time trend of $STDE_l$ in Figure 12, while the $THDG_h$ differs from $STDE_h$, due to the presence of a significant number of spikes resulting from the absence of proper damping factor information in the grouping evaluation. Note that in such a context the spikes are deleterious, because they prevent the localization of the real instants in which the high-frequency presence is maximum or minimum.

Eventually, Figure 45 shows the time trends of $THDG_l$ and $THDG_h$ evaluated for the transient waveform in case study 3 by means of SWMEM and using the same durations of the analysis windows utilized in the corresponding instantaneous approach.

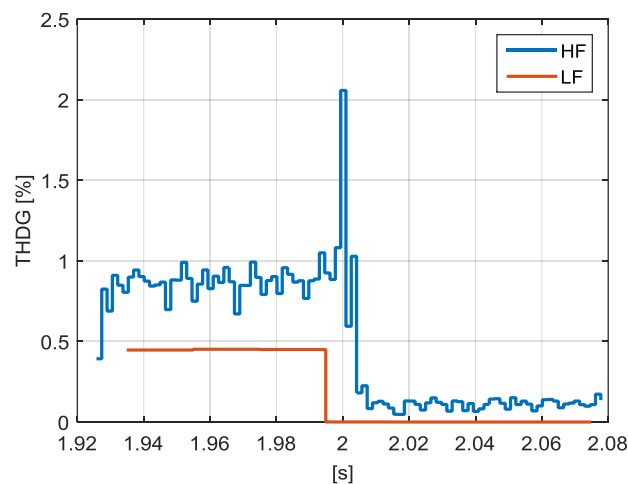


Figure 45. Case study 3: THDG at low-frequency ($0 \div 2.4$ kHz, red line) and at high-frequency ($2.4 \div 150$ kHz, blue line).

The time trend of the THDG at high-frequency in this case proves to properly localize the transient. Some problems could occur only in the presence of greater high-frequency distortions, where the possible presence of spikes could mask the net localization of the transient. At low-frequency, the THDG individuates a variation slightly before 2 s, but no peaks are detectable.

4.2. Modern Non-Linear Loads

Case Study 4

Three 0.2 s-current waveforms measured at the PCC of a fluorescent lamp installation were analyzed. Specifically, the three waveforms were recorded when one, ten and forty-eight fluorescent lamps were powered. All lamps were powered by high-frequency ballast. The total active power consumption of one lamp was about 0.1 kW. The current waveforms were measured with a Pearson current probe, model 411. The currents were sampled with 12-bit resolution and 10 MS/s sampling speed. Additionally, an anti-aliasing filter (a low-pass filter with a cut-off frequency 1 MHz) was utilized. More details on the installation structure, instrument specification and error verification of measurement are available in [12].

The analyzed currents are shown in Figure 46; the peak value of the currents grows with the number of supplied lamps, starting from less than 0.8 A for one lamp (Figure 46a), reaching almost 7 A in presence of ten lamps (Figure 46b) and reaching over 30 A when forty-eight lamps were supplied (Figure 46c). Note also that the high-frequency components on the peak of the waveform are clearly evident in Figure 46a (one lamp), while they become less visible as the number of supplied lamps increases (Figure 46b,c). This fact is better shown in Figure 47, where the high-frequency waveforms obtained by the DWT decompositions of the original waveforms in Figure 46 are presented.

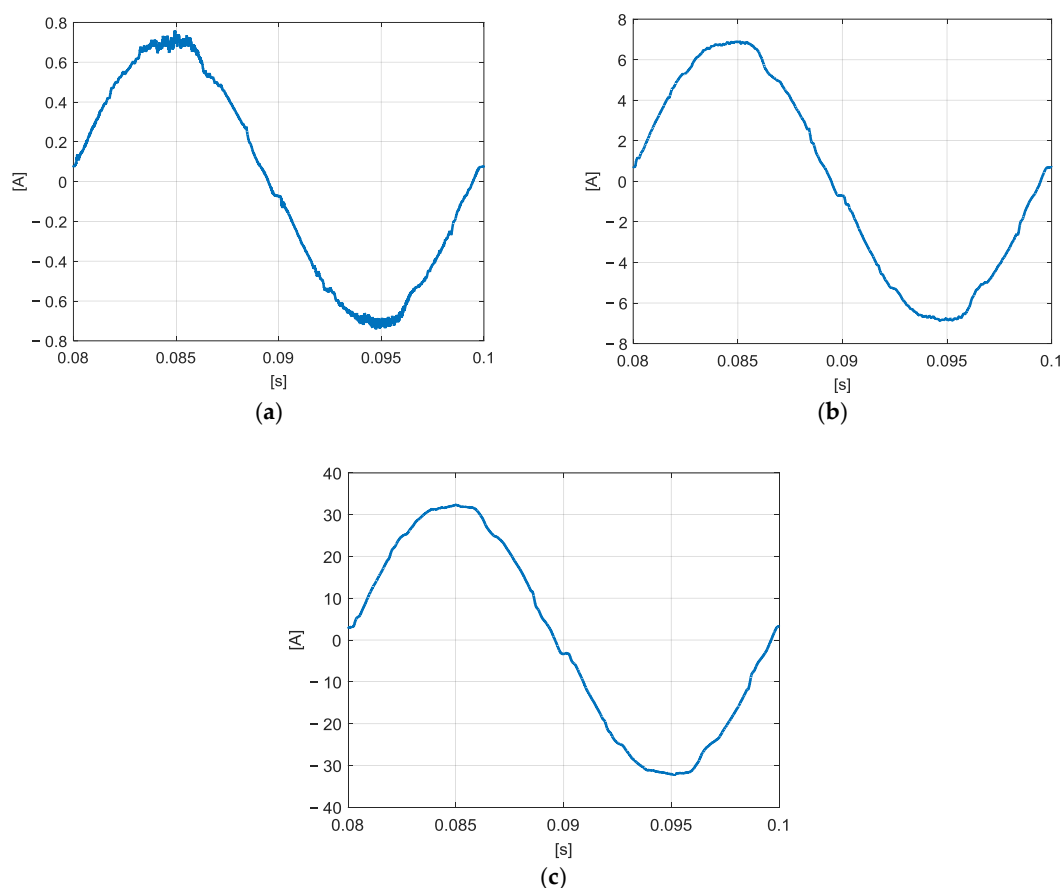


Figure 46. Case study 4: time trends of the waveforms under study, measured for (a) one lamp, (b) ten lamps, and (c) forty-eight lamps.

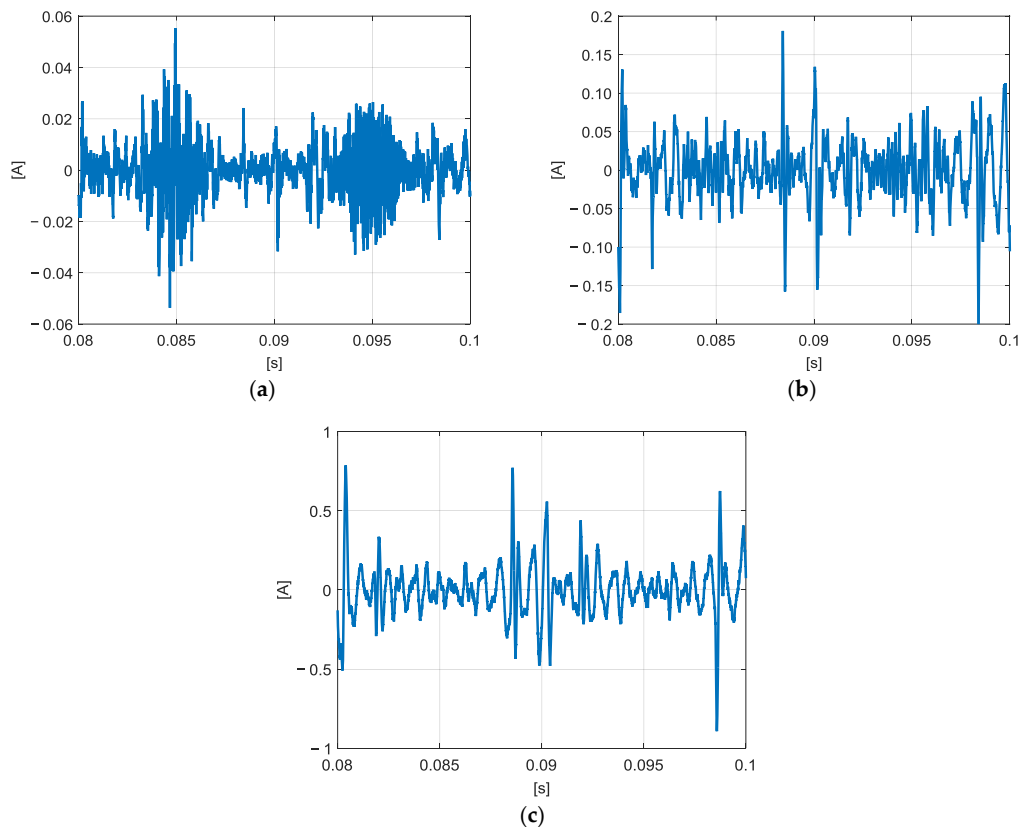


Figure 47. Case study 4: time trends of the high-frequency waveforms for (a) one lamp, (b) ten lamps, and (c) forty-eight lamps.

Also in Figure 47, the peak values grow as the number of supplied lamps increases, but the oscillations are simultaneously reduced. This implies that, as the number of lamps increases, some high-frequency components attenuate due to cancellation effect for their phase angle variations, while other high-frequency components increase due to their summation.

For the sake of brevity, the time trends of the low-frequency waveforms are not shown, since their behavior is well known.

In this case study, only the instantaneous approach was performed by means the SWWMEM, utilizing durations of time window equal to 0.04 s and to 0.5 ms for the analysis of the low-frequency and high-frequency waveforms, respectively. The analyses provide the results shown in Figures 48–50 in terms of proposed indices.

Specifically, Figure 48 shows the STDE at low-frequency (red lines) and at high-frequency (blue lines), evaluated for each of the three different currents under test. The STDE time trends clearly show that the low-frequency content grows almost proportionally as the fundamental component increases, since the $STDE_l$ values, globally, stay in the range between 0.035 p.u. and 0.04 p.u. Conversely, for high-frequency spectral content, the STDE time-trends vary more sharply as the number of supplied lamps varies. In fact, the peaks visible in Figure 48a (one lamp) become needles in Figure 48b (ten lamps) and they practically disappear in Figure 48c (forty-eight lamps). Simultaneously, the minimum values of $STDE_h$ also decrease as the number of powered lamps increases.

The previous remarks can also be easily extended to the $\Delta STFD$ trends in Figure 49. In particular, while the $\Delta STFD_l$ trends (red lines) change slightly as the number of supplied lamps varies, the $\Delta STFD_h$ trends (blue lines) provide three very different scenarios. In fact, the $\Delta STFD_h$ in Figure 49a (one lamp) reaches over 30 Hz, in Figure 49b (ten lamps), it doesn't exceed 7 Hz, and in Figure 49c (forty-eight lamps), it stays generally under 2 Hz.

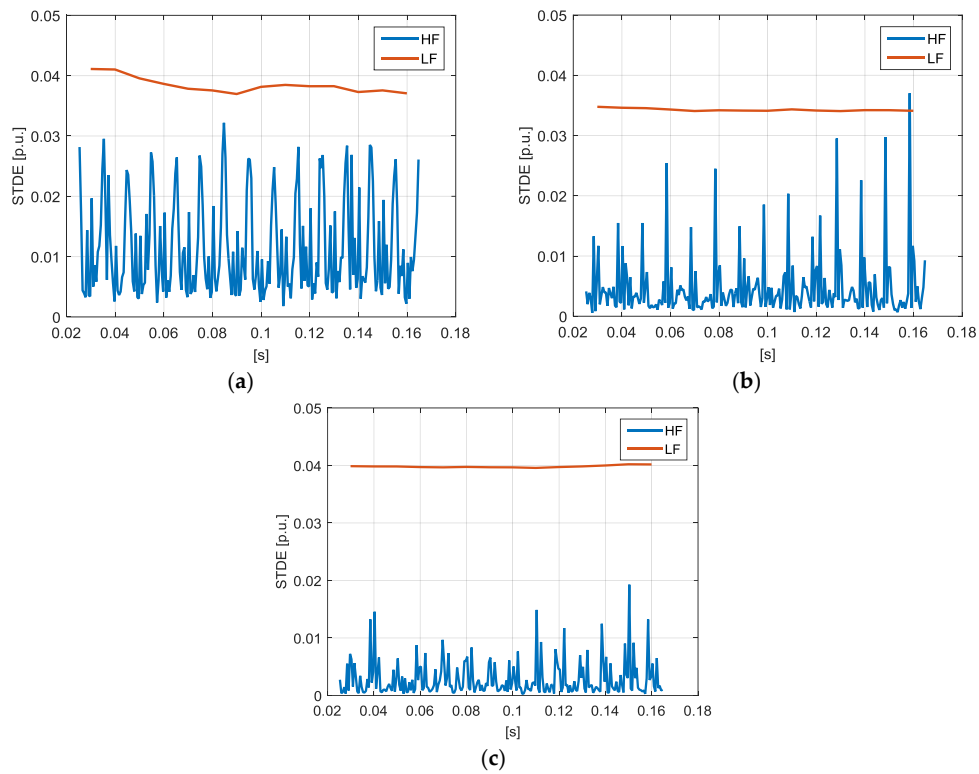


Figure 48. Case study 4: STDE at low-frequency (0 ÷ 2 kHz, red line) and at high-frequency (2 ÷ 150 kHz, blue line) obtained for (a) one lamp, (b) ten lamps, and (c) forty-eight lamps.

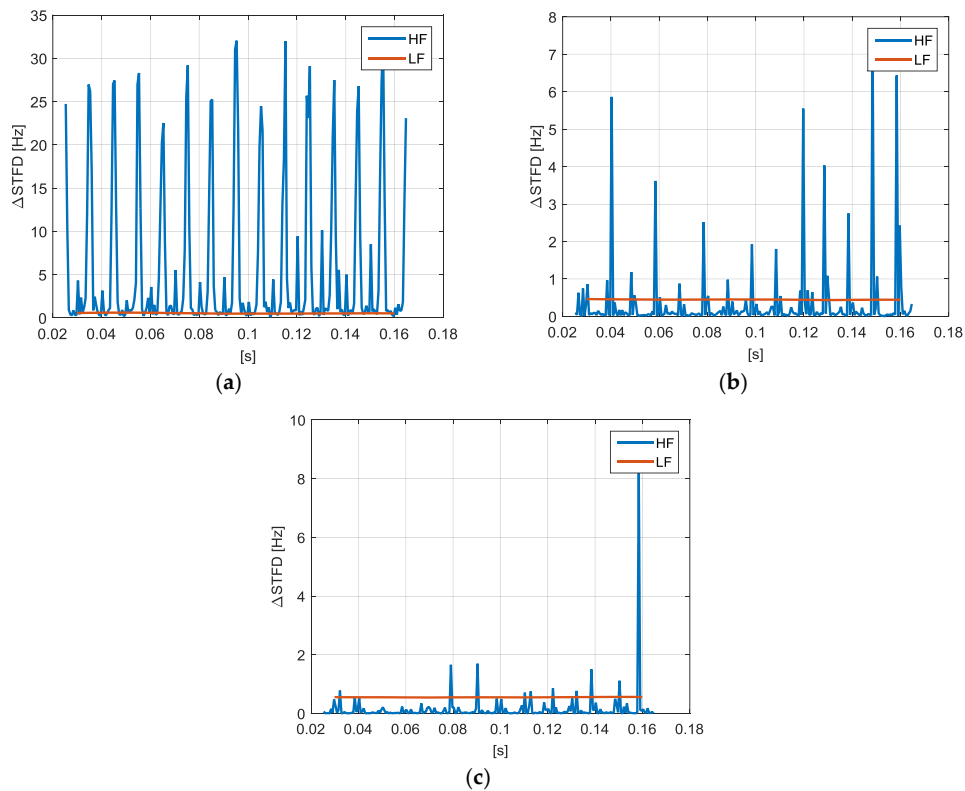


Figure 49. Case study 4: $\Delta STFD$ at low-frequency (0 ÷ 2 kHz, red line) and at high-frequency (2 ÷ 150 kHz, blue line) obtained for (a) one lamp, (b) ten lamps and (c) forty-eight lamps.

Coherently, in Figure 50 the ΔSTK trends show for the high-frequency components (blue lines) shorter and increasingly rare peaks as the number of lamps grows, while for the low-frequency (red lines), the time trend variations is negligible.

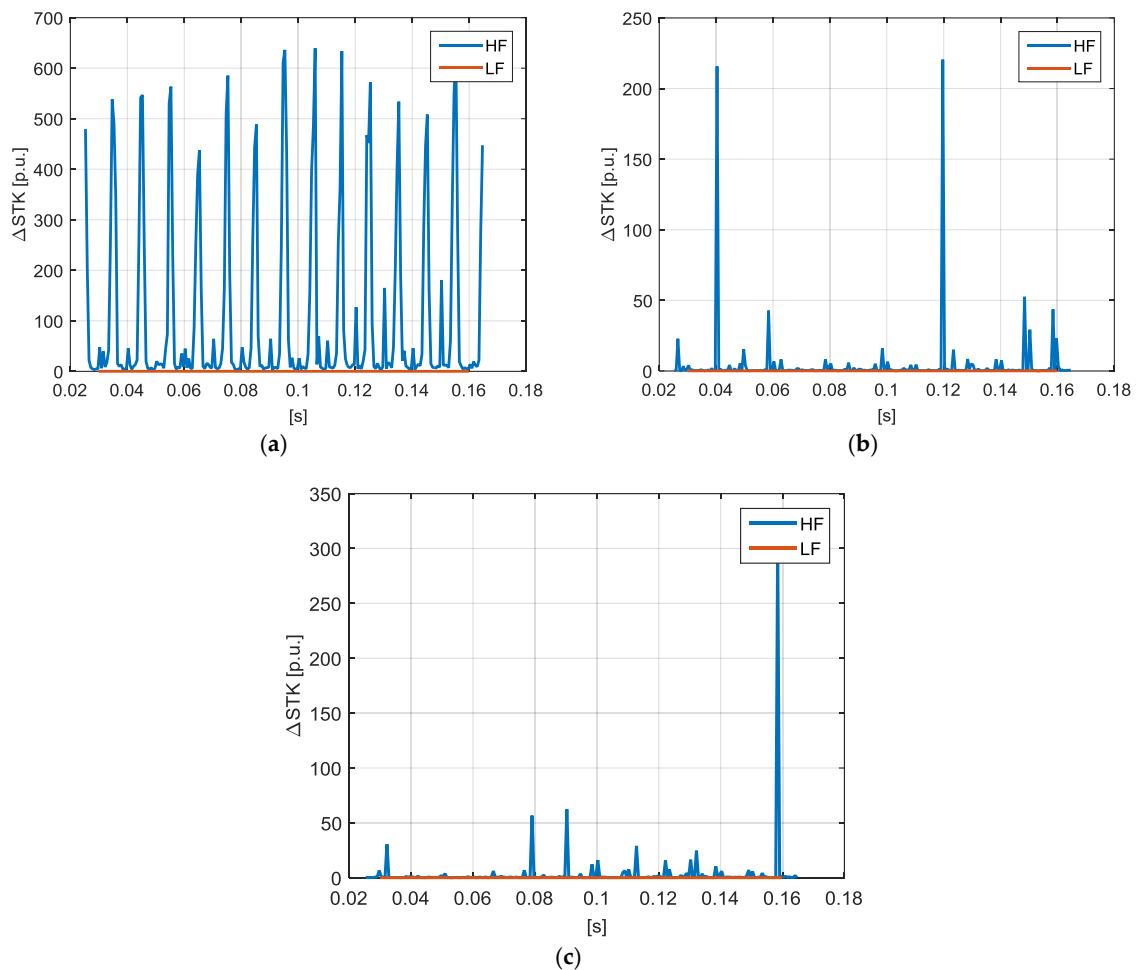


Figure 50. Case study 4: ΔSTK at low-frequency ($0 \div 2$ kHz, red line) and at high-frequency ($2 \div 150$ kHz, blue line) obtained for (a) one lamp, (b) ten lamps, and (c) forty-eight lamps.

4.3. Final Discussion on the Obtained Results

The results obtained in the considered case studies revealed that the proposed indices, evaluated through SWWEM, well describe both stationary and transient time-varying spectral components at low- and high-frequency, especially utilizing the instantaneous approach.

In particular, case studies 1 and 2 tested the performances of the proposed indices in the presence of different wide spectra under stationary conditions. In these two cases, similar behavior and trends could be observed in all of the corresponding indices, with the only difference being in the peak values, growing as the spectral component amplitudes and/or frequencies increase. Specifically, the aforesaid case studies present low-frequency indices as almost constant, and high-frequency indices are characterized by periodical time trends. Moreover, while the $STDE_l$ trends are higher than those of the $STDE_h$ indices (Figures 4 and 12), the values assumed by $\Delta STFD_l$ and ΔSTK_l appear to be significantly lower than those of both $\Delta STFD_h$ and ΔSTK_h (Figures 5, 6, 13 and 14). This is in line with the definitions of the proposed indices, since it underscores the fact that, for the first two considered case studies, the energy of the low-frequency spectral content was predominant with respect to the energy of the high-frequency spectral content ($STDE_l > STDE_h$), but, weighting these energies with the frequencies or the squared normalized frequencies, the effects of high-frequency range became

predominant. The late approach provides averaged values of the instantaneous approach for all of the high-frequency proposed indices.

The third case study examines the performances of the proposed indices during a transient. In this case, with the instantaneous approach, each typology of proposed indices provides peak values corresponding to the transient, both at low- and high-frequency time trends, and it assumes an almost constant value before and after the transient. However, it is worth observing that the transient is detectable by means of the proposed indices, as a couple of peaks both at low- and high-frequency can be individuated; its detailed localization is provided only by the peak at high-frequency, since the localization of the event becomes more accurate as the duration of the sliding-window decreases. Note also that the distortion level is different before and after the transient; specifically, as shown in Figure 19, the distortion level decreases after the transient, due to an increased value of the fundamental component. Finally, in this case study, $\Delta STFD_l$ is higher than $\Delta STFD_h$, demonstrating that relevant variations also occur in the spectral content at low-frequency during the transient. Once again, the late approach provides averaged values of the instantaneous approach for all of the high-frequency proposed indices, masking any peaks. This means that the transient can be individuated by utilizing the late approach, but it cannot be accurately localized.

The proposed indices in the first three case studies were also calculated with STFT (Figures 25–27, 31–33 and 37–39) and Prony methods (Figures 28–30, 34–36 and 40–42). Both methods provide, at their best, results that are similar to the late approach of SWWMEM, but often they suffer from the high sampling rate and the presence of a wide spectrum to be analyzed using a single analysis window, so the results become unreliable. In addition, the Group Total Harmonic Distortions (THDGs) at low- and high-frequency were also calculated (Figures 43–45). Their time trends prove to be generally coherent with those of $STDE_l$ and $STDE_h$, but THDGs could often suffer from the presence of spikes, highlighting fake peak values, making it unclear if corrective actions are required to avoid problems for a specific installation. Moreover, transient detection by means of the THDGs proved to be slightly more difficult than with the proposed indices. In fact, $THDG_h$ properly localizes the transient, but problems could occur in the presence of more elevated high-frequency distortions or spikes. The $THDG_l$ individuates a variation slightly before 2 s, but no peaks are detectable.

Finally, in the last case study, the instantaneous approach performed by SWWMEM was utilized for the compared evaluation of the proposed indices in the presence of different numbers of perturbing devices connected to the PCC. In this case, one, ten and forty-eight lamps were selected, showing that the proposed indices are also able to underscore and individuate the combinative effects (cancellation and sum) of the spectral content caused by multiple disturbing sources.

5. Conclusions

In this paper, we propose new PQ indices that specifically address the evaluation of waveform distortions in the presence of both low-frequency and high-frequency spectral content.

In particular, starting from the current lack of standardization for the supraharmmonic range, some of the PQ indices presented in the relevant literature were modified, utilizing the decomposition of wide-spectrum waveforms and the subsequently separated spectral analysis of each frequency range offered by the sliding-window wavelet-modified ESPRIT method (SWWMEM).

The proposed PQ indices are:

- (i) the short time disturbance energy index evaluated both for the low-frequency and high-frequency range ($STDE_l$ and $STDE_h$);
- (ii) the short time frequency deviation difference index evaluated both for the low-frequency and high-frequency distortions ($\Delta STFD_l$ and $\Delta STFD_h$);
- (iii) the short time k-factor difference index evaluated both for the low-frequency and high-frequency distortions (ΔSTK_l and ΔSTK_h).

The aforementioned proposed indices proved to be useful tools for the characterization of problems (e.g., overheating, equipment malfunctioning, losses due to skin effects, hysteresis losses or eddy current losses) resulting from the presence of both low-frequency and high-frequency distortions.

Numerical experiments were performed both on synthetic and measured waveforms related to photovoltaic system operations. For the first two considered waveforms (stationary conditions), the high-frequency disturbances, although associated with almost negligible amplitudes, proved to determine comparable or higher losses than the low-frequency distortions.

A sensitivity analysis was also performed in order to observe the effect of the selected duration of the analysis window on the evaluation of the proposed indices for high-frequency disturbances. This sensitivity analysis demonstrates that the choice of a very-short analysis window could be particularly suitable in situations where an instantaneous detection of the extent of the problems related to high-frequency distortions needs to be effected. Using a larger analysis window, only smoothed and averaged information on the problem's extent is able to be obtained. Eventually, as observed in the numerical applications, the instantaneous approach is also able to provide the information obtainable from the late approach, while the opposite, as is obvious, does not hold. However, although the instantaneous approach is preferable to the late approach, the latter could be particularly suitable when a reduced amount of data needs to be stored, and a rough characterization of the waveform is acceptable.

Also, for the third waveform, referred to as the transient condition, the maximum advantages are obtained by means of the instantaneous approach. In fact, in this case, the transient is univocally individuated by each type of proposed index as a couple of peaks (at low- and high-frequency); its detailed localization is provided by the peak at high-frequency.

Moreover, the proposed indices for the first three case studies have also been evaluated by means of STFT and Prony's method. Both methods suffer from the elevated sampling rate, and the analysis of the whole wide spectrum, so the obtained results become unreliable. In addition, the analysis of the whole waveform does not allow the use of different sliding windows in different frequency bands (instantaneous and late approach).

Finally, the THDG indices at low- and high-frequency were estimated, once again, for the first three case studies. However, the presence of spikes was able to introduce fake peak values in these indices, adding uncertainty to the need for corrective operations in order to protect a specific installation.

Eventually, the fourth case study provides the comparison of the proposed PQ indices evaluated by means the instantaneous SWWMEM approach with reference to three currents measured at the PCC when one, ten and forty-eight lamps were powered. The aim was to underscore that the proposed PQ indices may also be good tools for the evaluation of the combinative effects (cancellation and sum) of spectral content due to multiple disturbing sources connected to the PCC.

Note that the proposed indices should be general in nature, since they can be applied for the characterization of both component emissions and waveform distortions in the grid (including PCC). However, in the numerical application of this paper, if only motivated by the availability of measurements, we started to investigate the emissions at component level. Anyway, measurements and studies involving waveforms at PCC are in progress, and they will be subject of future works. This will allow to deeply investigate the influence of the network impedance.

Acknowledgments: This work was supported by the University of Napoli Parthenope in the framework of "Bando per il Sostegno alla Ricerca individuale per il triennio 2015–2017" and by the Swedish Energy Agency.

Author Contributions: Authors contributed equally to the entire paper.

Conflicts of Interest: The authors declare no conflict of interest.

Appendix A

The sliding-window wavelet-modified ESPRIT method (SWWMEM) is a two-step procedure articulated as follows [4]:

- (i) in the first step, the original waveform $x(n)$ to be analyzed is decomposed in a low-frequency waveform $x_l(n)$ and in a high-frequency waveform $x_h(n)$ by means of a discrete wavelet transform (DWT) [13];
- (ii) in the second step, the aforesaid two waveforms are properly resampled and analyzed separately by the sliding-window modified ESPRIT method (SW MEM) [27].

Specifically, in the first step, SWWMEM exploits the decomposition of the waveforms on different levels achieved by means of the DWT. If the waveform $x(n)$ is sampled at $2f_{\max}$ Hz, with f_{\max} the maximum frequency of interest (i.e., 150 kHz), and f_{bs} is the bands' separation frequency (i.e., 2 kHz), the number L_{max} of decomposition levels to be performed is $L_{max} = \left\lceil \log_2 \left(\frac{f_{\max}}{f_{bs}} \right) \right\rceil$. At each level, the approximation a_j and the detail d_j of the waveform in progressively-halved bands of frequency are obtained as the inverse DWTs of the approximate $A_j(k)$ and detailed $D_j(k)$ coefficients, computed as follows:

$$\begin{aligned} D_j(k) &= \frac{1}{\sqrt{a_0^j}} \sum_{n=0}^{N-1} x(n) \psi^* \left(\frac{n-k}{a_0^j} \right) \\ A_j(k) &= \frac{1}{\sqrt{a_0^j}} \sum_{n=0}^{N-1} x(n) \varphi^* \left(\frac{n-k}{a_0^j} \right) \end{aligned} \quad (A1)$$

where $\psi^* \left(\frac{n-k}{a_0^j} \right)$ and $\varphi^* \left(\frac{n-k}{a_0^j} \right)$ are the complex conjugates of the selected mother wavelet and of the corresponding scaling function, respectively, a_0^j is the discretized scale parameter, k is related to the translation in time and j is related to the selected frequency band [12].

In performing the DWT decomposition, the waveform $x_l(n)$ is obtained as the approximation $a_{L_{max}-1}$ at the level $L_{max} - 1$, while the waveform $x_h(n)$ is obtained as the sum of all of the details d_j .

In the second step of SWWMEM, the SWMEM described in [27] is applied for the separate assessment of the low-frequency and high-frequency components included in $x_l(n)$ and $x_h(n)$, respectively.

Let $x_i(n)$, of generic size L_i , be either the sequence of the L_l -sized sampled data $x_l(n)$ or the sequence of the L_h -sized sampled data $x_h(n)$, the ESPRIT model approximates each sample with a linear combination of M_i complex exponentials added to a white noise $r(n)$ [4,13,27]:

$$\hat{x}_i(n) = \sum_{k=1}^{M_i} A_{ik} e^{j\psi_{ik}} e^{(\alpha_{ik} + j2\pi f_{ik})nT_{si}} + r(n), \quad n = 0, 1, \dots, L_i - 1, \quad i = l, h, \quad (A2)$$

with obvious meaning of each symbol.

As described in [4,27], in SWMEM the frequencies and damping factors are considered piecewise constant, so their evaluation is performed only a reduced number of times along the whole waveform to be analyzed. In particular, these parameters are evaluated for each spectral component in only a few sliding windows (also called "basis windows"), properly generated according the outcomes of a check on the reconstruction error, which has to be lower than a selected threshold. In the other sliding windows (also called "no-basis windows"), the frequencies and damping factors are assumed to be known quantities, and their values are equal to those obtained in the previous basis window. The reduction of the unknown parameters thus obtained in the no-basis window provides a great improvement in terms of computational effort required for the spectral analysis, although the result accuracy typical of the parametric methods is also guaranteed [4,27].

Finally, note also that the duration of the analysis window for $x_h(n)$ is shorter than that of $x_l(n)$, so SWWMEM provides more high-frequency spectra than low-frequency spectra. This is in line with modern requirements in terms of higher time resolution for the detection of the high-frequency components, which vary in time more significantly than low-frequency components.

References

1. Meyer, J.; Bollen, M.; Amaris, H.; Blanco, A.M.; Gil de Castro, A.; Desmet, J.; Klatt, M.; Kocewiak, Ł.; Rönnberg, S.; Yang, K. Future work on harmonics—Some expert opinions Part II—Supraharmonics standards and measurements. In Proceedings of the 16th IEEE International Conference on Harmonics and Quality of Power (ICHQP), Bucharest, Romania, 25–28 May 2014.
2. International Council on Large Electrical Systems (CIGRE). *Impact of Increasing Contribution of Dispersed Generation on the Power System*; CIGRE WG 37–23; International Council on Large Electrical Systems (CIGRE): Paris, France, 1999.
3. Ribeiro, P. *Time-Varying Waveform Distortions in Power Systems*; John Wiley & Sons: New York, NY, USA, 2009.
4. Alfieri, L.; Bracale, A.; Carpinelli, G.; Larsson, A. A Wavelet-Modified ESPRIT Hybrid Method for Assessment of Spectral Components from 0 to 150 kHz. *Energies* **2017**, *10*, 97. [[CrossRef](#)]
5. Moreno-Munoz, A.; Gil-de-Castro, A.; Romero-Cavadal, E.; Rönnberg, S.; Bollen, M. Supraharmonics (2 to 150 kHz) and multi-level converters. In Proceedings of the IEEE 5th International Conference on Power Engineering, Energy and Electrical Drives (POWERENG), Riga, Latvia, 11–13 May 2015; pp. 37–41.
6. International Special Committee on Radio Interference. *CISPR 15: Limits and Methods of Measurement of Radio Disturbance Characteristics of Electrical Lighting and Similar Equipment*; International Special Committee on Radio Interference: Geneva, Switzerland, 2013.
7. International Electrotechnical Commission (IEC). *IEC Standard 61000–4-7: General Guide on Harmonics and Interharmonics Measurements, for Power Supply Systems and Equipment Connected Thereto*; International Electrotechnical Commission (IEC): Geneva, Switzerland, 2010.
8. International Electrotechnical Commission (IEC). *IEC Standard 61000–4-30: Testing and Measurement Techniques—Power Quality Measurement Methods*; International Electrotechnical Commission (IEC): Geneva, Switzerland, 2015.
9. Larsson, E.O.A.; Bollen, M.H.J.; Wahlberg, M.G.; Lundmark, C.M.; Rönnberg, S.K. Measurements of high frequency (2–150 kHz) distortion in low-voltage networks. *IEEE Trans. Power Deliv.* **2010**, *25*, 1749–1757. [[CrossRef](#)]
10. Bollen, M.; Olofsson, M.; Larsson, A.; Rönnberg, S.; Lundmark, M. Standards for supraharmonics (2 to 150 kHz). *IEEE Electromagn. Compat. Mag.* **2014**, *3*, 114–119. [[CrossRef](#)]
11. Rönnberg, S.K.; Bollen, M.H.J.; Amaris, H.; Chang, G.W.; Gu, I.Y.H.; Kocewiak, Ł.H.; Meyer, J.; Olofsson, M.; Ribeiro, P.F.; Desmet, J. On waveform distortion in the frequency range of 2 kHz–150 kHz—Review and research challenges. *Electr. Power Syst. Res.* **2017**, *150*, 1–10. [[CrossRef](#)]
12. Alfieri, L.; Bracale, A.; Carpinelli, G.; Larsson, A. Accurate Assessment of Waveform Distortions up to 150 kHz due to Fluorescent Lamps. In Proceedings of the 6th International Conference on Clean Electrical Power (ICCEP), Santa Margherita Ligure, Liguria, Italy, 27–29 June 2017.
13. Caramia, P.; Carpinelli, G.; Verde, P. *Power Quality Indices in Liberalized Markets*; Wiley-IEEE Press: Chippenham, UK; Wiltshire, UK, 2009.
14. Rönnberg, S.; Bollen, M. Power quality issues in the electric power system of the future. *Electr. J.* **2016**, *29*, 49–61. [[CrossRef](#)]
15. Andreotti, A.; Bracale, A.; Caramia, P.; Carpinelli, G. Adaptive Prony Method for the Calculation of Power-Quality Indices in the Presence of Nonstationary Disturbance Waveforms. *IEEE Trans. Power Deliv.* **2009**, *24*, 874–883. [[CrossRef](#)]
16. Shin, Y.; Powers, E.J.; Grady, M.; Arapostathis, A. Power quality indices for transient disturbances. *IEEE Trans. Power Deliv.* **2006**, *21*, 253–261. [[CrossRef](#)]
17. Emanuel, A.; McEachern, A. Electric power definitions: A debate. In Proceedings of the IEEE Power & Energy Society (PES) General Meeting, Vancouver, BC, Canada, 21–25 July 2013.
18. Larsson, E.O.A.; Bollen, M.H.J. Measurement result from 1 to 48 fluorescent lamps in the frequency range 2 to 150 kHz. In Proceedings of the 14th International Conference on Harmonics and Quality of Power (ICHQP), Bergamo, Italy, 26–29 September 2010; pp. 1–8.
19. Yazdani, A.; Di Fazio, A.R.; Ghoddami, H.; Russo, M.; Kazerani, M.; Jatskevich, J.; Strunz, K.; Leva, S.; Marinez, J.A. Modeling guidelines and a benchmark for power system simulation studies of three-phase single-stage photovoltaic systems. *IEEE Trans. Power Deliv.* **2011**, *26*, 1247–1264. [[CrossRef](#)]

20. Renner, H.; Heimbach, B.; Desmet, J. Power quality and electromagnetic compatibility: Special report session 2. In Proceedings of the 23rd International Conference and Exhibition on Electricity CIRED, Lyon, France, 15–18 June 2015.
21. Li, H.; Chen, Z. Overview of different wind generator systems and their comparisons. *IET Renew. Power Gener.* **2008**, *2*, 123–138. [[CrossRef](#)]
22. Blaabjerg, F.; Iov, F.; Chen, Z.; Ma, K. Power electronics and controls for wind turbine systems. In Proceedings of the 2010 IEEE International Energy Conference and Exhibition (EnergyCon), Manama, Bahrain, 18–22 December 2010.
23. Alfieri, L. Some advanced parametric methods for assessing waveform distortion in a smart grid with renewable generation. *EURASIP J. Adv. Signal Process.* **2015**, *2015*, 1–16. [[CrossRef](#)]
24. Bracale, A.; Caramia, P.; Carpinelli, G.; Di Fazio, A.R. Modeling the three-phase short-circuit contribution of photovoltaic systems in balanced power systems. *Int. J. Electr. Power Energy Syst.* **2017**, *93*, 204–215. [[CrossRef](#)]
25. Bracale, A.; Caramia, P.; Carpinelli, G.; Rapuano, A. A New, Sliding-Window Prony and DFT Scheme for the Calculation of Power-Quality Indices in the Presence of Non-stationary Waveforms. *Int. J. Emerg. Electr. Power Syst.* **2012**, *13*, 112–120. [[CrossRef](#)]
26. Gallo, D.; Landi, C.; Luiso, M. AC and DC power quality of photovoltaic systems. In Proceedings of the IEEE International Instrumentation and Measurement Technology Conference (I2MTC), Graz, Austria, 13–16 May 2012; pp. 576–581.
27. Alfieri, L.; Carpinelli, G.; Bracale, A. New ESPRIT-based method for an efficient assessment of waveform distortions in power systems. *Electr. Power Syst. Res.* **2015**, *122*, 130–139. [[CrossRef](#)]



© 2017 by the authors. Licensee MDPI, Basel, Switzerland. This article is an open access article distributed under the terms and conditions of the Creative Commons Attribution (CC BY) license (<http://creativecommons.org/licenses/by/4.0/>).